NASA/ TP- 20260008467

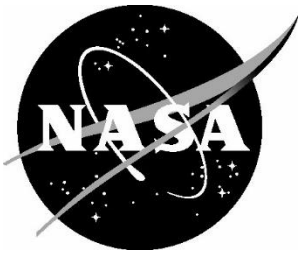

Scale-Up, Mechanical Evaluation, and Hardware Demonstration of the NASA HR-2 Superalloy Fabricated by Laser Powder Bed Fusion for Hydrogen-Sensitive Liquid Rocket Engine Applications

Po-Shou Chen, Hunter T. Ray, Diana Y. Andreev, Robert Lamdin,
Amentum ESSCA Group, Huntsville, Alabama

Colton C. Katsarelis, Anthony W. Jones, Chin H. Su, Paul W. Northrop, Thomas G. Hayes, Vann Bradford
Marshall Space Flight Center, Huntsville, Alabama

September 2026

Since its founding, NASA has been dedicated to the advancement of aeronautics and space science. The NASA scientific and technical information (STI) program plays a key part in helping NASA maintain this important role.

The NASA STI program operates under the auspices of the Agency Chief Information Officer. It collects, organizes, provides for archiving, and disseminates NASA's STI. The NASA STI program provides access to the NTRS Registered and its public interface, the NASA Technical Reports Server, thus providing one of the largest collections of aeronautical and space science STI in the world. Results are published in both non-NASA channels and by NASA in the NASA STI Report Series, which includes the following report types:

- TECHNICAL PUBLICATION. Reports of completed research or a major significant phase of research that present the results of NASA Programs and include extensive data or theoretical analysis. Includes compilations of significant scientific and technical data and information deemed to be of continuing reference value. NASA counterpart of peer-reviewed formal professional papers but has less stringent limitations on manuscript length and extent of graphic presentations.

- TECHNICAL MEMORANDUM. Scientific and technical findings that are preliminary or of specialized interest, e.g., quick release reports, working papers, and bibliographies that contain minimal annotation. Does not contain extensive analysis.

- CONTRACTOR REPORT. Scientific and technical findings by NASA-sponsored contractors and grantees.

- CONFERENCE PUBLICATION. Collected papers from scientific and technical conferences, symposia, seminars, or other meetings sponsored or co-sponsored by NASA.

- SPECIAL PUBLICATION. Scientific, technical, or historical information from NASA programs, projects, and missions, often concerned with subjects having substantial public interest.

- TECHNICAL TRANSLATION. English-language translations of foreign scientific and technical material pertinent to NASA's mission.

Specialized services also include organizing and publishing research results, distributing specialized research announcements and feeds, providing information desk and personal search support, and enabling data exchange services.

For more information about the NASA STI program, see the following:

- Access the NASA STI program home page at http://www.sti.nasa.gov

.

NASA/ TP- 20260008467

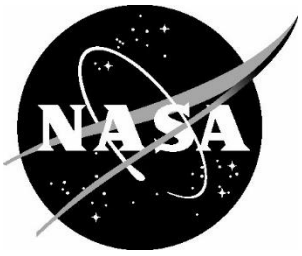

Scale-Up, Mechanical Evaluation, and Hardware Demonstration of the NASA HR-2 Superalloy Fabricated by Laser Powder Bed Fusion for Hydrogen-Sensitive Liquid Rocket Engine Applications

Po-Shou Chen, Hunter T. Ray, Diana Y. Andreev, Robert Lamdin,
Amentum ESSCA Group, Huntsville, Alabama

Colton C. Katsarelis, Anthony W. Jones, Chin H. Su, Paul W. Northrop, Thomas G. Hayes, Vann Bradford
Marshall Space Flight Center, Huntsville, Alabama

National Aeronautics and Space Administration

Marshall Space Flight Center
Huntsville, AL

September 2026

September 2026

Table of Contents

List of Figures

List of Tables

List of Abbreviations, Acronyms and Symbols

AM	additive manufacturing
Ar	argon
CAD	computer-aided design
da/dN	fatigue crack growth rate (da/dN)
FCC	face-centered cubic
FE	field emission
GH_2	gaseous hydrogen
HCF	high-cycle fatigue
HEE	hydrogen environment embrittlement
HIP	hot isostatic pressing
HPOTP	high-pressure oxidizer turbopump
HR-2	Hydrogen Restistant-2
IPS	interpropellant seal
KIC	fracture toughness
LCF	low-cycle fatigue
LH_2	liquid hydrogen
LN_2	liquid nitrogen
L-PBF	laser powder bed fusion
LPFTP	low-pressure fuel turbopump
LRE	liquid rocket engine
LSG	low-stress grinding
MSFC	Marshall Space Flight Center
n	strain-hardening exponent
NASA	National Aeronautics and Space Administration

Ni-Fe	Nickel-Iron
Ra	arithmetic average roughness of a 2D surface profile
Sa	arithmetic mean height of a 3D surface area
RT	room temperature
SEM	scanning electron microscopy
S-N	stress-number of cycle
Ti	titanium
TIPI	Technology, Innovation, and Process Improvement
UTS	ultimate tensile strength
VED	volumetric energy density
YS	yield strength

1.0 Introduction

Additive manufacturing (AM) continues to play a critical role in enabling advanced space propulsion systems by providing opportunities for cost reduction, schedule compression, part consolidation, and performance optimization. In liquid hydrogen (LH_2) propulsion systems, however, the application of AM has been limited by the susceptibility of many high-strength alloys to hydrogen environment embrittlement (HEE) when exposed to high-pressure gaseous hydrogen (GH_2) [1, 2]. To address this challenge, NASA has pursued the development of AM-optimized, hydrogen-resistant materials specifically tailored for liquid rocket engine (LRE) applications [3–9].

In Phase I of this effort, NASA Hydrogen Resistant-2 (HR-2), a nickel-iron (Ni-Fe)-based, γ′-strengthened superalloy, was successfully developed for fabrication by laser powder bed fusion (L-PBF) [10, 11]. Phase I activities focused on alloy design, L-PBF process development, post-build heat treatment optimization, and comprehensive microstructural and mechanical characterization. The results demonstrated that L-PBF NASA HR-2 exhibits excellent printability, high strength and ductility, and exceptional resistance to hydrogen environment embrittlement, including minimal degradation in tensile properties during testing in 5-ksi GH_2 environments. These achievements established NASA HR-2 as a promising material for hydrogen-exposed LRE components and advanced the technology to a laboratory-validated readiness level [10, 11].

Building upon the successful completion of Phase I, Phase II transitions from material development to technology maturation through heat treatment optimization, high-cycle fatigue evaluation, hardware-focused demonstrations, and process scale-up. The primary objective of this phase is to assess the fatigue performance of L-PBF NASA HR-2 and demonstrate the fabrication and evaluation of hydrogen-relevant LRE hardware representative of flight-like components. A key element of this effort is the transition from a small-format prototyping platform (EOS M100) to a mid-scale production system (EOS M290), enabling the manufacture of larger and more geometrically complex components relevant to operational propulsion systems.

Phase II activities include the fabrication of full-scale RS-25 engine hardware using L-PBF NASA HR-2 to demonstrate manufacturability, scalability, and performance for hydrogen-service applications. Demonstration hardware includes representative low-pressure fuel turbopump (LPFTP) components, including lift-off seals, turbine wheels, pump shafts, second-stage rotors, and the mixer located in the RS-25 nozzle. These components were selected to represent a range of geometric complexities, loading conditions, and hydrogen exposure environments, providing a comprehensive assessment of process capability, design limits, and material performance at a production-relevant scale. Concurrent process optimization and mechanical testing in both ambient air and hydrogen environments were conducted to further enhance material performance and evaluate process robustness as component size and build complexity increased.

Through process scale-up, full-scale hardware fabrication, and continued material and mechanical evaluation, Phase II activities are intended to mature L-PBF NASA HR-2 from laboratory validation (TRL 4) to system-relevant hardware demonstration (TRL 6). Successful completion of this effort will establish NASA HR-2 as a uniquely capable hydrogen-resistant superalloy compatible with L-PBF manufacturing and provide a viable pathway for the application of additive manufacturing to hydrogen-sensitive liquid rocket engine components.

Phase II development of L-PBF NASA HR-2 was funded through grants provided by Amentum's Technology, Innovation, and Process Improvement (TIPI) program and the Liquid Engine Office at NASA's Marshall Space Flight Center (MSFC).

2.0 Experimental Procedures and Methods

2.1 Material

Two alloy formulations (Formulations I and II) were evaluated during Phase I development of L-PBF NASA HR-2 using an EOS M100 system [10, 11]. Compared with Formulation I, Formulation II exhibited lower porosity, a higher degree of recrystallization, and slightly improved fracture elongation in hydrogen environments. Based on these results, Formulation II was selected for the Phase II study conducted using an EOS M290 system.

The material used in the present study was pre-alloyed NASA HR-2 powder supplied by Linde (Indianapolis, IN, USA). The analyzed chemical composition of the NASA HR-2 powder, together with the nominal specification for Formulation II, is summarized in Table 1. The measured composition generally satisfied the specified ranges for the major alloying elements. However, the Ti content was slightly below the specified minimum, and the Si content exceeded the specified maximum. The reduced Ti level is expected to slightly decrease precipitation strengthening, whereas the influence of elevated Si on microstructural evolution and mechanical performance has not been established for this alloy system and was not explicitly investigated in the present study. The powder was accepted in the as-received condition because remanufacturing would have required several months and significantly delayed the project schedule.

Table 1. Analyzed chemical composition (wt%) of NASA HR-2 powder and nominal specification limits for Formulation II.

Wt.%	**NASA HR-2 Formulation II**			
Element	**Analyzed**	**Nominal**	**Min**	**Max**
Ni	BAL	BAL	-	-
Fe	30.48	30	29	31
Cr	15.39	15.5	14.75	16.25
Co	3.83	4	3.5	4.5
Mo	3.02	3	2.7	3.3
W	3.34	3.2	2.95	3.45
Ti	2.53	2.8	2.55	3.05
Al	0.28	0.25	0.2	0.3
S	0.001	-	-	0.01
P	<0.005	-	-	0.01
C	0	-	-	0.03
Si	0.13	-	-	0.05
B	<0.001	-	-	0.005
Mn	0.01	-	-	0.05
H	6 ppm	-	-	<50 ppm
O	240 ppm	-	-	<300 ppm
N	24 ppm	-	-	<200 ppm

The specified powder size distribution was 10–45 μm (+325/−1250 mesh). Powder morphology was characterized using a Hitachi scanning electron microscope (SEM) operated at an accelerating voltage of 15 kV. Representative SEM images of the NASA HR-2 powder are shown in Figure 1. The powder particles were predominantly spherical, with occasional satellite particles observed. These satellites are believed to form during gas atomization when rapidly solidified fine particles adhere to partially molten or semi-solid larger particles as a result of in-flight particle collisions [12].

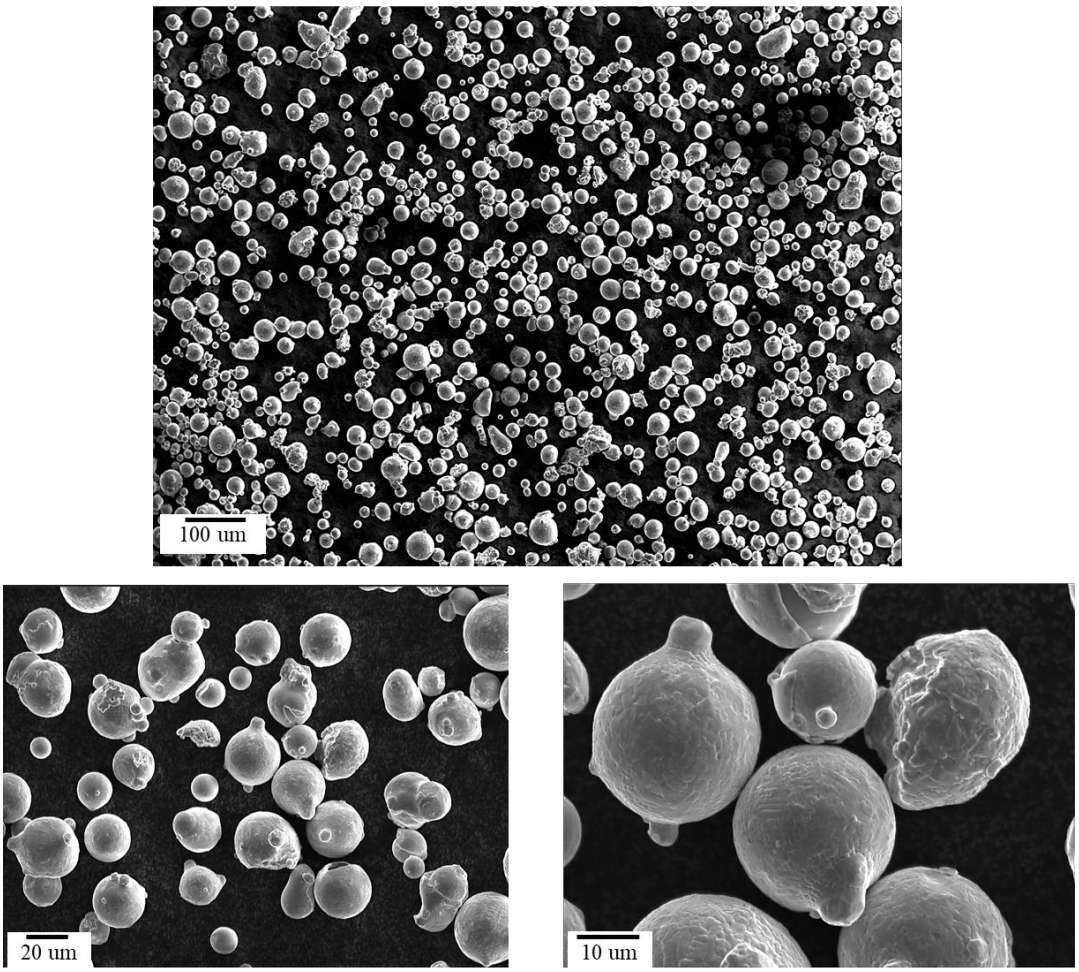

Figure 1. SEM images showing the particle morphology of NASA HR-2 powder (Formulation II).

2.2 Laser Powder Bed Fusion (L-PBF) Process

L-PBF fabrication of NASA HR-2 specimens was performed using an EOS M290 system at NASA MSFC. The EOS default scan strategy was employed, which incorporates layer-wise re-melting and a nominal 67° hatch rotation between successive layers. The rotating hatch pattern changes the heat-flow direction from layer to layer and has been shown to promote more randomized grain orientations, thereby reducing crystallographic texture and microstructural anisotropy through disruption of epitaxial grain growth [13].

On the EOS M290 platform, restrictions are imposed to prevent laser scanning parallel to the argon gas-flow direction (y-direction). When the nominal 67° hatch rotation would produce scan vectors within ±30° of the gas-flow direction, that rotation is skipped and an additional 67° rotation is applied instead [14].

The scan area was partitioned using the EOS default stripe-based strategy, in which each layer was divided into approximately 10 mm-wide stripes with a nominal overlap of 0.12 mm to limit continuous scan-vector length. Key L-PBF process parameters included laser power, scan speed, hatch spacing, and layer thickness. Process parameter development was conducted to identify conditions capable of producing dense, defect-minimized HR-2 components.

2.3 Heat Treatment

Following L-PBF fabrication, all specimens underwent a common post-processing heat-treatment sequence consisting of stress relief at 1950°F for 1.5 h, hot isostatic pressing (HIP) at 2125°F and 15 ksi for 3 h, solution annealing at 2050°F for 1 h, and argon quenching. An aging study was then conducted to evaluate the effects of single-step and two-step aging treatments on room-temperature tensile properties. The aging conditions investigated are summarized in Table 2. The resulting tensile properties are presented in Section 3.4.1.

For applications requiring compliance with minimum yield-strength requirements, a two-step aging treatment consisting of 1325°F for 16 h followed by 1150°F for 16 h was required. This condition produced a yield strength of approximately 105–106 ksi while maintaining acceptable ductility.

Table 2. Summary of aging treatments evaluated for L-PBF NASA HR-2.

Material	Aging Treatment No.	Aging Treatment Schedule
L-PBF NASA HR-2	1	1325 °F/16h
	2	1325 °F/16h + 1150 °F/16h
	3	1300 °F/16h + 1150 °F/16h
	4	1300 °F/16h + 1200 °F/16h
	5	1275 °F/16h + 1150 °F/16h
	6	1275 °F/16h + 1200 °F/16h

2.4 Metallography and Scanning Electron Microscopy (SEM) Analysis

Selected L-PBF NASA HR-2 specimens were metallographically characterized in the as-built condition and following heat treatment and mechanical testing. Specimens were sectioned, mounted, ground, and polished using standard metallographic procedures, including sequential

220–2000 grit SiC papers, followed by polishing with a 3 μm diamond suspension and final polishing with a 0.05 μm alumina suspension.

Chemical etching was performed using waterless Kalling's reagent with an immersion time of 5–10 s. Fresh acetic glyceregia was used to reveal melt-pool morphology in the as-built condition. Microstructural characterization of as-built and heat-treated specimens was performed using optical microscopy (Leica DMi8 A) and scanning electron microscopy (SEM, Hitachi S-3700N). High-resolution optical montage images were acquired to document microstructural features across the full specimen cross section.

Fractographic analysis of selected high-cycle fatigue (HCF)-tested specimens was conducted using an FEI field-emission (FE) SEM to characterize fatigue crack initiation sites and crystallographic slip features associated with early-stage fatigue crack propagation.

2.5 Mechanical Testing

Tensile testing was performed in ambient laboratory air at a nominal strain rate of 0.05 in/in/min over a temperature range of −423 °F to 1200 °F. Elevated-temperature tensile tests were conducted using an Instron load frame equipped with a 250 kN load cell and a Mayes elevated-temperature extensometer (Model R3/8 Block 2), in accordance with ASTM E21. Room-temperature (RT) tensile testing was performed using an Instron 5582 load frame with a 100 kN load cell and an Instron Model 2620 extensometer in accordance with ASTM E8.

Tensile testing was also conducted at ambient temperature in a 5 ksi gaseous hydrogen (GH_2) environment. The geometry of the smooth tensile specimens used for testing in ambient air and high-pressure gas environments is shown in Figure 2. All specimens had a uniform gauge section with a diameter of 0.25 in and a gauge length of 1.25 in. For specimens tested in hydrogen, the final gauge-section machining was performed using low-stress grinding (LSG) in accordance with ASTM G142. The specified arithmetic mean surface roughness was $Ra \leq 32$ μin.

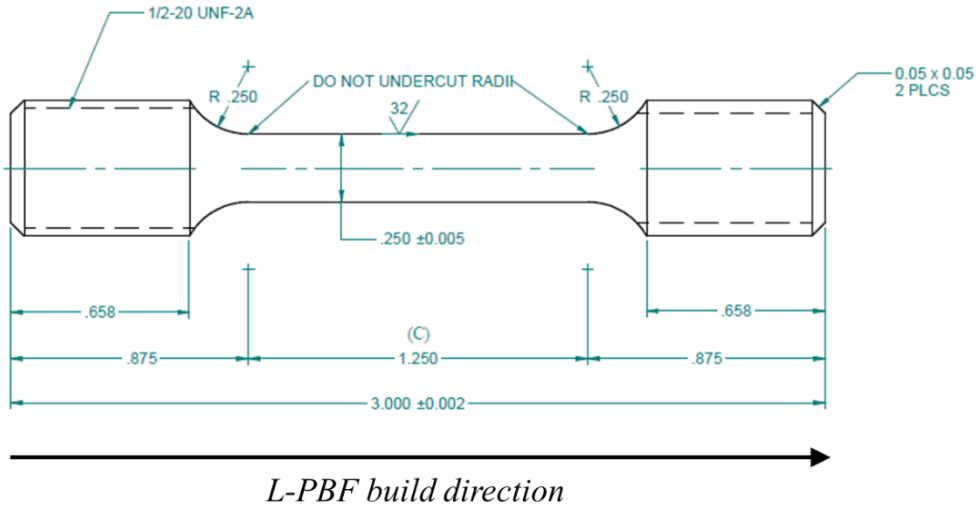

Figure 2. Geometry and dimensions of the smooth tensile specimen used for testing in ambient air and in 5 ksi gaseous hydrogen at ambient temperature. All dimensions are in inches. For hydrogen-tested specimens, the gauge section was finished using low-stress grinding to achieve a surface finish of Ra ≤ 32 µin.

Smooth tensile testing in hydrogen was conducted to failure at a pre-yield strain rate of 0.005 in/in/min [7]. The strain rate was determined using a system-specific calibration that correlated actuator stroke rate with the effective specimen strain rate, accounting for machine compliance and fixture deformation. All reported strain rates represent calibrated pre-yield specimen strain rates.

Fracture elongation was determined from extensometer measurements. Susceptibility to hydrogen environment embrittlement (HEE) was assessed using relative fracture elongation, defined as the ratio of fracture elongation measured in high-pressure GH_2 to that measured in ambient air.

Tension–tension (R = 0.1) and fully reversed tension–compression (R = −1) HCF testing was conducted in ambient laboratory air at room temperature under stress-controlled conditions. The R = 0.1 tests were performed under tensile cyclic loading with a non-zero mean stress, whereas the R = −1 tests were conducted under fully reversed loading conditions ($\sigma_{max} = -\sigma_{min}$).

Based on the room-temperature tensile properties of L-PBF HR-2 (YS ≈ 100–105 ksi), HCF stress levels were selected as fractions of the yield strength to ensure predominantly elastic cyclic

loading and avoid significant cyclic plasticity. The selected stress range encompassed both the fatigue transition and long-life regimes. All tests were conducted at 25 Hz (1500 cycles/min).

Specimens had a nominal gauge diameter of 0.25 in and were machined by turning to achieve a final surface roughness of approximately 8 µin Ra or better. The geometry of the HCF specimens is shown in Figure 3. All HCF testing was conducted in accordance with ASTM E466.

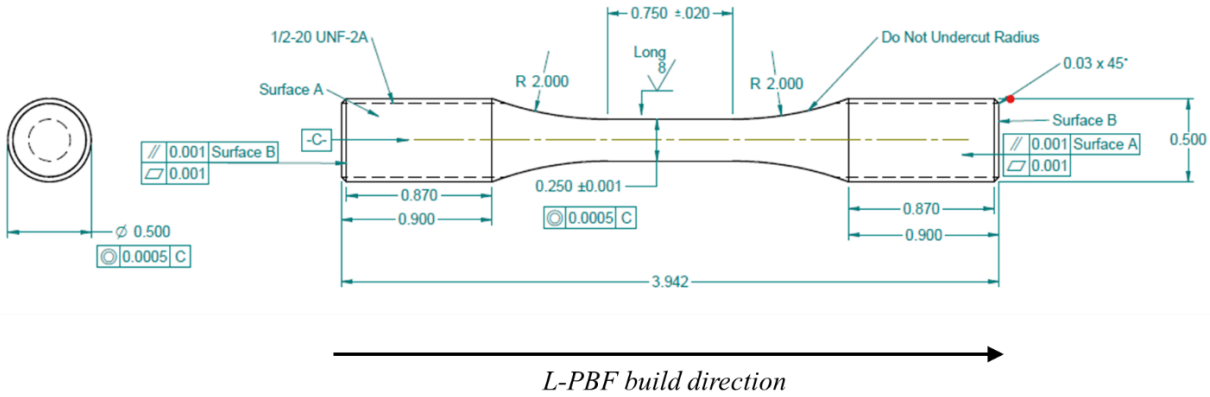

Figure 3. Geometry of the smooth specimen used for HCF testing in ambient air. All dimensions are in inches. The reduced section (C) was finish-machined to final diameter by turning.

3.0 Results and Discussion

3.1 Phase Diagram

The isopleth phase diagram of NASA HR-2, calculated using Thermo-Calc, is shown in Figure 4. An isopleth represents a vertical section through a multicomponent phase diagram in which all component concentrations are held constant except for one variable. In the present study, the titanium (Ti) content was varied from 2.0 to 3.0 wt%, while all other alloying elements were maintained at their nominal compositions. NASA HR-2 is a Ni-Fe-based superalloy containing approximately 30 wt% Fe, with Ni as the balance. The isopleth was constructed to evaluate the influence of Ti content on phase stability and to support heat-treatment development.

Figure 4 illustrates the evolution of the equilibrium phase assemblage as a function of Ti content and temperature. At elevated temperatures, the γ phase (face-centered cubic [FCC]) is the stable matrix phase. Upon cooling, secondary phases, including the η phase (Ni_3Ti), become thermodynamically stable. The η phase is a brittle intermetallic compound that can degrade ductility, toughness, and fatigue resistance, particularly in hydrogen-containing environments where resistance to HEE is critical [6].

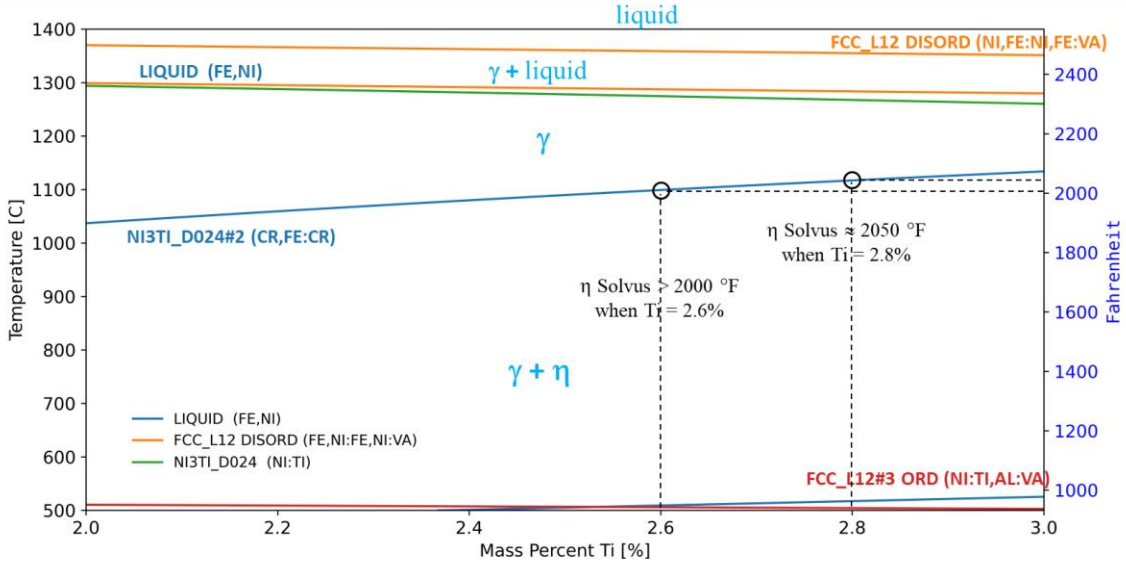

Figure 4. Isopleth phase diagram of NASA HR-2 as a function of titanium content (2.0–3.0 wt%) at the nominal alloy composition (Fe ≈ 30 wt%, Ni balance). All other alloying elements were maintained at their nominal values listed in Table 1.

Under equilibrium conditions, the phase diagram predicts that the η phase becomes stable at temperatures near 2000 °F when the Ti content exceeds approximately 2.6 wt%. For the nominal NASA HR-2 composition containing 2.8 wt% Ti, η-phase stability begins at approximately 2050 °F. These results suggest that L-PBF-processed NASA HR-2, particularly material near the upper limit of the Ti specification range, may be susceptible to η-phase formation due to microsegregation associated with rapid solidification and the resulting local compositional variations.

The formation of η phase is undesirable because it can adversely affect ductility, low-cycle fatigue (LCF) resistance, and resistance to hydrogen-assisted degradation [6]. Consequently, a primary objective of the post-build solution annealing treatment is to dissolve any η phase present and restore a single-phase γ matrix. The calculated isopleth indicates that, for compositions near 2.8 wt% Ti, solution annealing temperatures above approximately 2050 °F are required to completely eliminate the η phase under equilibrium conditions. This prediction provided the basis for selecting the solution annealing temperatures evaluated during heat-treatment optimization.

Overall, the isopleth phase diagram provides a useful framework for understanding phase stability, interpreting microstructural evolution, and guiding post-processing strategies for L-PBF NASA HR-2 components.

3.2 Laser Powder Bed Fusion (L-PBF) Parameter Development

3.2.1 Core Parameter Development

Fifteen L-PBF parameter sets were evaluated to establish a processing window for NASA HR-2 (Table 3). The parameter matrix varied scan speed (880–1300 mm/s) and hatch spacing (0.11–0.13 mm), while laser power (285 W) and layer thickness (0.04 mm) were maintained constant.

These variations produced a wide range of volumetric energy density (VED), with parameter set 285-11-P4 representing the highest energy input condition and 285-12-5 representing the lowest. Relative build efficiency was assessed using the estimated exposure time required to fabricate a 100 mm × 100 mm area (Table 3).

Table 3. L-PBF process parameters used for fabrication of parameter development samples. Relative processing time denotes the estimated exposure time required to for 100 mm × 100 mm area.

	Laser Power (W)	Scan Speed (mm/s)	Hatch Spacing (mm)	Layer Thickness (mm)	VED (J/mm^3)	Est Exposure time of 100mm x 100mm
285-11-P4	285	960	0.11	0.04	67.47	94.697
285-11-P5	285	1020	0.11	0.04	63.50	89.127
285-11-P6	285	1100	0.11	0.04	58.88	82.645
285-11-P7	285	1150	0.11	0.04	56.32	79.051
285-11-P8	285	1200	0.11	0.04	53.98	75.758
285-12-1	285	1020	0.12	0.04	58.21	81.699
285-12-2	285	1080	0.12	0.04	54.98	77.160
285-12-3	285	1140	0.12	0.04	52.08	73.099
285-12-4	285	1200	0.12	0.04	49.48	69.444
285-12-5	285	1300	0.12	0.04	45.67	64.103
285-13-1	285	880	0.13	0.04	62.28	87.413
285-13-2	285	920	0.13	0.04	59.57	83.612
285-13-3	285	960	0.13	0.04	57.09	80.128
285-13-4	285	1020	0.13	0.04	53.73	75.415
285-13-5	285	1080	0.13	0.04	50.75	71.225

The objective of this study was to identify processing conditions that maximize part quality while maintaining acceptable build efficiency, capturing the inherent trade-off between energy input, consolidation behavior, and productivity in L-PBF processing. Resulting specimens were characterized for relative density and microstructural evolution to establish process–structure relationships and define an optimized processing window.

3.2.1.1 Porosity Analysis

Porosity was measured in both as-built and HIP conditions across all parameter sets (Table 4). NASA HR-2 exhibited low as-built porosity (<0.05%) across most evaluated conditions, demonstrating a relatively broad processing window and strong inherent printability.

Table 4. As-built and HIP-ed porosity of L-PBF NASA HR-2 as a function of VED.

Specimen ID	% Porosity-a-built	% Porosity after HIP	VED (J/mm^3)
285-11-P4	0.0102	0.0084	67.47
285-11-P5	0.0214	0.0191	63.50
285-11-P6	0.0389	0.0327	58.88
285-11-P7	0.0662	0.0652	56.32
285-11-P8	0.0455	0.0956	53.98
285-12-1	0.0342	0.0231	58.21
285-12-2	0.0733	0.0668	54.98
285-12-3	0.0773	0.0746	52.08
285-12-4	0.1037	0.1012	49.48
285-12-5	0.240	0.0921	45.67
285-13-1	0.0254	0.0227	62.28
285-13-2	0.0185	0.0191	59.57
285-13-3	0.0302	0.0209	57.09
285-13-4	0.0436	0.0224	53.73
285-13-5	0.0498	0.0323	50.75

Porosity variation is governed primarily by scan speed, hatch spacing, and VED, which collectively control melt pool stability and inter-track fusion quality. These parameters define the consolidation behavior and establish a processing window characterized by minimized lack-of-fusion defect formation. Representative optical micrographs of the as-polished, as-built microstructure are shown in Figure 5.

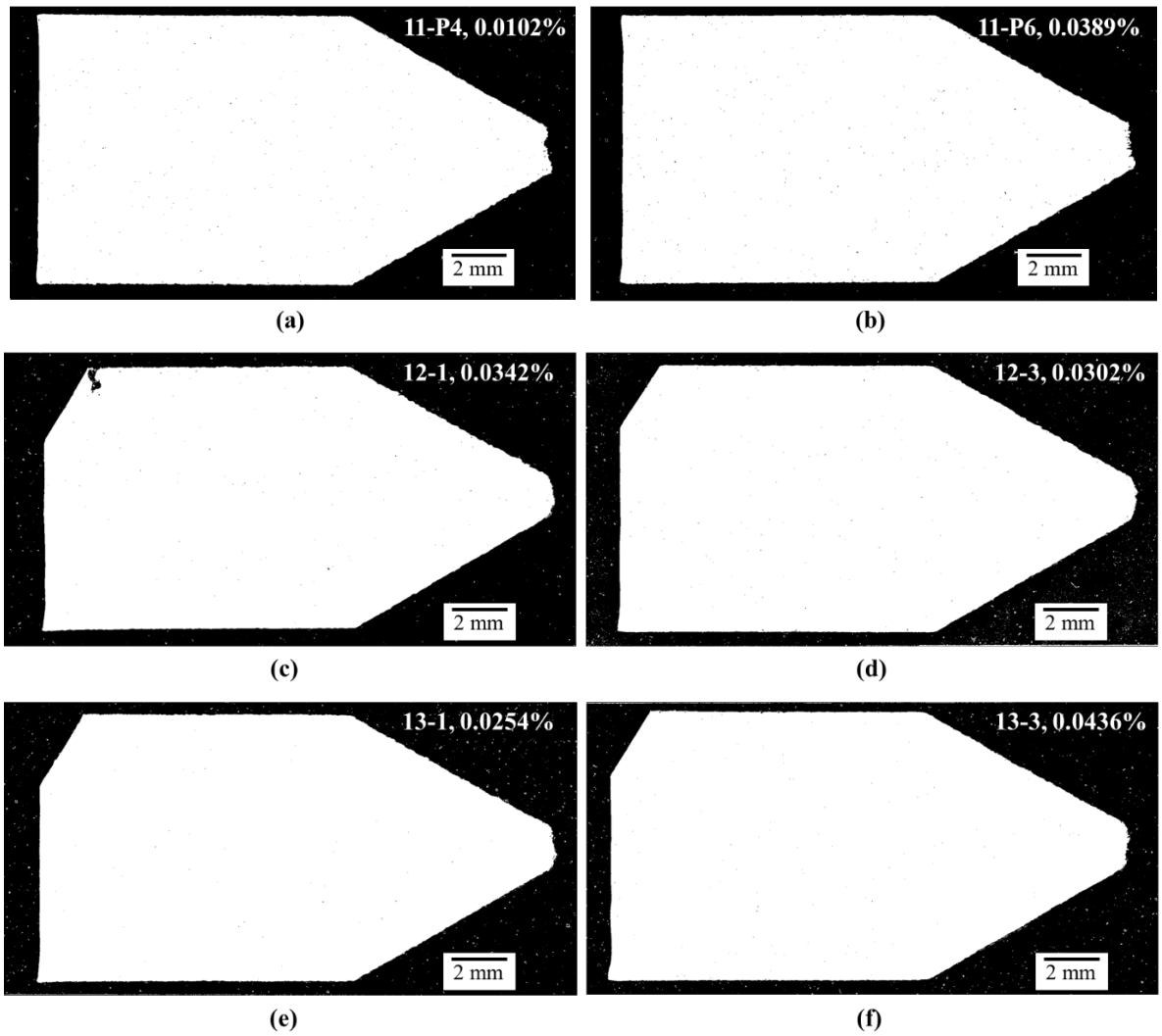

Figure 5. Optical micrographs of L-PBF NASA HR-2 in the as-polished, as-built condition. Six representative build conditions are shown and grouped by hatch spacing: (a–b) 0.11 mm (285-11-P4, 285-11-P6); (c–d) 0.12 mm (285-12-1, 285-12-3); and (e–f) 0.13 mm (285-13-1, 285-13-3), spanning the evaluated VED range of 52–67 J/mm³.

3.2.1.2 Effects of Process Parameters

Porosity trends for as-built and HIP conditions are shown in Figure 6. HIP reduces residual porosity across all process conditions, with the magnitude of reduction governed by the initial defect population.

In the as-built condition, porosity is controlled by scan speed, hatch spacing, and VED, which collectively determine melt pool stability and track overlap. Although VED provides a useful

indicator of overall energy input, the results demonstrate that scan strategy variables, particularly hatch spacing and melt pool overlap, strongly influence consolidation behavior.

Hatch spacing = 0.11 mm

A hatch spacing of 0.11 mm provides increased track overlap and stable melt pool behavior. Minimum porosity (0.010%) was observed in specimen 285-11-P4 (960 mm/s, 67.5 J/mm³). Low porosity (<0.05%) is maintained across 1020–1100 mm/s, indicating a broad and stable processing window. At scan speeds ≥1150 mm/s, porosity increases due to reduced overlap and lack-of-fusion formation.

Hatch spacing = 0.12–0.13 mm

Increased hatch spacing reduces inter-track overlap and narrows the stable processing window. At comparable scan conditions, porosity increases relative to 0.11 mm spacing (e.g., 285-12-2 vs. 285-11-P5). Although low porosity is achievable, sensitivity to process variation increases.

Process interaction

Scan speed and VED jointly define the consolidation regime. Low scan speeds increase energy input and may promote keyhole instability, while high scan speeds increase susceptibility to lack-of-fusion defects. Among all conditions evaluated, 0.11 mm hatch spacing provides the most robust low-porosity processing window.

Based on combined porosity and stability considerations, parameter sets 285-11-P5 and 285-11-P6 were selected for hardware fabrication.

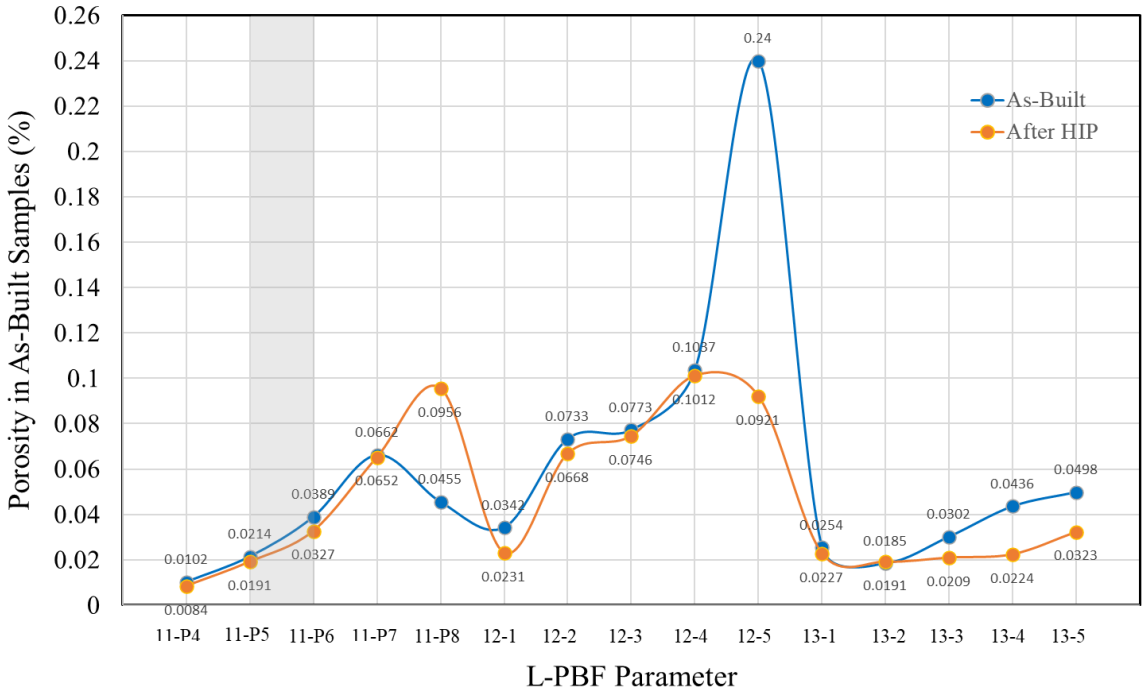

Figure 6. Porosity of L-PBF NASA HR-2 as a function of process parameter ID for as-built and HIP-ed conditions. The shaded region indicates the selected processing window (285-11-P5 and 285-11-P6) used for hardware fabrication.

3.2.1.3 Effect of Hot Isostatic Pressing (HIP) Treatment

HIP significantly reduces residual porosity in L-PBF NASA HR-2 (Figure 6). For specimens with low as-built porosity (<0.05%), post-HIP porosity decreases to ~0.02%, indicating effective closure of fine, isolated pores associated with gas entrapment and solidification shrinkage.

HIP effectiveness is strongly dependent on defect morphology, with isolated gas/shrinkage porosity readily reduced, while lack-of-fusion defects exhibit limited closure due to irregular, interconnected geometry [15]. In well-consolidated material, porosity is predominantly small, near-spherical, and isolated, enabling diffusion-driven closure under elevated temperature and isostatic pressure.

In contrast, specimens containing lack-of-fusion defects (e.g., 285-12-5) retain measurable porosity after HIP due to persistent crack-like pore networks and restricted diffusion pathways.

Gas-entrapment pores may also exhibit limited closure when internal gas pressure counteracts the applied isostatic stress.

Consequently, HIP produces the greatest densification improvement in well-consolidated material, with effectiveness decreasing as lack-of-fusion defect severity increases.

3.2.2 Downskin Parameter Development

Downskin parameter optimization is a critical aspect of L-PBF because overhanging surfaces are fabricated above unconsolidated powder rather than fully dense material. The low thermal conductivity and limited mechanical support provided by the powder bed alter melt pool behavior, increasing susceptibility to dross formation, sagging, balling, and geometric stair-stepping. As a result, downskin surfaces typically exhibit higher roughness than upward-facing or vertical surfaces and often require dedicated processing parameters to achieve acceptable surface quality [16].

Optimized downskin conditions are particularly important for internal flow passages and other complex geometries where post-processing access is limited. Appropriate combinations of laser power, scan speed, and hatch spacing can improve melt pool stability, reduce powder adhesion, and minimize Sa while maintaining dimensional accuracy.

In this study, 45° downskin Sa was evaluated using a factorial combination of three core (infill) parameter sets—285-11-P4, 285-11-P5.1, and 285-12-1—and nine downskin parameter sets (D1, D3, D5, D6, D7, D11, D14, D15, and D20). The geometry of the downskin specimens is shown in Figure 7. The objective was to identify a core-downskin parameter combination that minimizes Sa while maintaining metallurgical quality suitable for flight hardware fabrication.

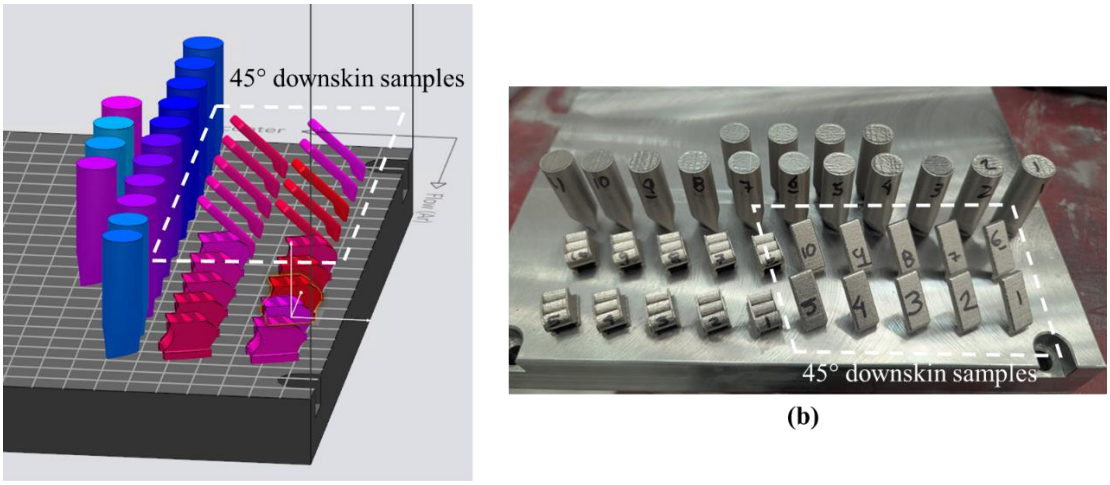

(a) (b)

Figure 7. (a) Computer-aided design (CAD) model of the 45° downskin specimen used for parameter evaluation. (b) Additively manufactured downskin specimens fabricated for Sa characterization.

The three core (infill) parameter sets evaluated are summarized in Table 5. These parameters establish the baseline thermal history, consolidation behavior, and microstructural condition of the builds and therefore influence the response of the downskin surfaces to the applied downskin parameters. The average downskin Sa values reported in Table 5 represent the mean Sa measured across all nine downskin parameter sets (shown in Table 6) and provide a comparative assessment of core parameter performance.

Table 5. Core (infill) parameter sets evaluated for downskin optimization.

Core Parameter Set	Laser Power (watt)	Scan Speed (mm/s)	Hatch Spacing (mm)	Layer Thickness (mm)	VED	Avg Sa (µm) of 9 Downskin Parameters
285-11-P4	285	960	0.11	0.04	67.47	42.2
285-11-P5.1	285	1060	0.11	0.04	61.11	38.2
285-12-1	285	1020	0.12	0.04	58.21	43.8

Note: Average Sa values represent the mean 45° downskin Sa measured for each core parameter set across all nine downskin parameter conditions.

Each core parameter set was subsequently combined with the same nine downskin parameter sets to evaluate 45° downskin Sa. The resulting Sa measurements for all core-downskin parameter combinations are summarized in Table 6, which enables direct comparison of downskin

performance across different core conditions and supports identification of parameter sets suitable for demonstration hardware fabrication.

Table 6. Effect of core and downskin parameter combinations on 45° downskin surface roughness (Sa).

Downskin Parameter						45° Downskin Sa (μm)		
Parameter ID	Laser Power (watt)	Scan Speed (mm/s)	Hatch Spacing (mm)	Layer Thickness(mm)	VED	285-11-P4 Core	285-11-P5.1 Core	285-12-1 Core
D1	95	850	0.1	0.04	27.94	45.07	41.08	55.96
D3	95	950	0.1	0.04	25.00	43.93	32.60	43.14
D5	95	1100	0.1	0.04	21.59	37.29	38.83	47.33
D6	120	850	0.1	0.04	35.29	54.23	31.51	46.42
D7	120	1100	0.1	0.04	27.27	41.95	47.58	52.88
D11	95	1100	0.1	0.04	21.59	32.4	33.02	40.70
D14	95	1400	0.1	0.04	16.96	38.23	39.71	38.84
D15	75	620	0.1	0.04	30.24	43.41	32.21	33.31
D20	75	1100	0.1	0.04	17.05	43.34	48.10	35.72

Note 1: Core parameter sets: 285-11-P4 (VED = 67.47 J·mm⁻³), 285-11-P5.1 (VED = 61.11 J·mm⁻³), and 285-12-1 (VED = 58.21 J·mm⁻³); corresponding process parameters are listed in Table 5.

Note 2: D5 and D11 were fabricated using identical downskin parameters and are treated as duplicate builds for assessment of process and measurement repeatability.

3.2.2.1 Key Observations

3.2.2.1.1 Effect of Downskin Parameters

Figure 8 summarizes the effect of downskin parameter set on Sa for each core condition. Low downskin Sa was consistently achieved using parameter sets D5/D11, D14, and D15.

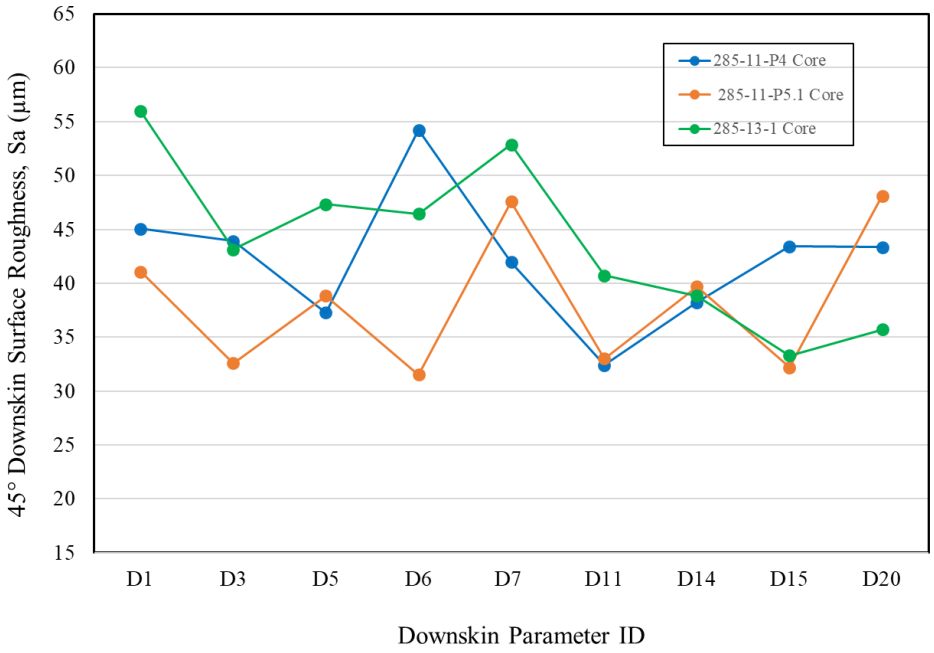

Figure 8. Effect of downskin parameter set on 45° downskin Sa for the three evaluated core parameter conditions. Each point represents the average Sa for a given downskin parameter set with a specific core condition.

Because D5 and D11 were fabricated using identical processing parameters, differences in measured roughness represent combined fabrication and measurement variability rather than parameter effects. The generally low roughness values obtained for both builds indicate good repeatability of the selected downskin condition. Across the three core parameter sets, the duplicate D5/D11 builds differed by approximately 5–7 µm Sa, indicating reasonable repeatability of both the fabrication process and Sa measurements. In contrast, D3, D6, and D20 exhibited greater variability across the evaluated core parameter sets (Table 6).

Figure 9 illustrates the relationship between downskin VED and 45° downskin Sa for the three evaluated core parameter conditions. No clear or monotonic correlation between VED and Sa was observed.

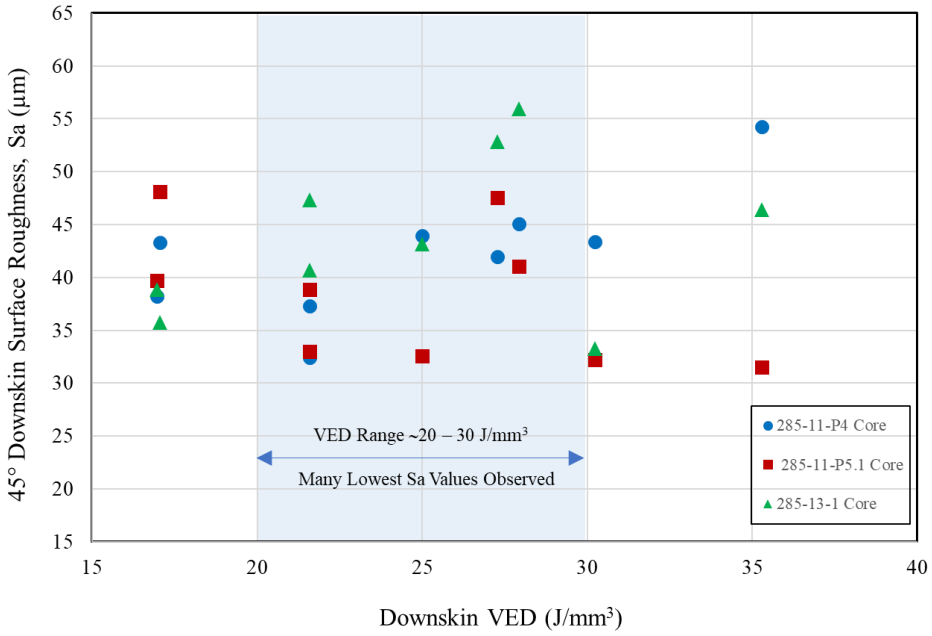

Figure 9. Relationship between downskin VED and 45° downskin Sa for the three evaluated core parameter conditions. D5 and D11 were fabricated using identical processing parameters (VED = 21.59 J/mm³). Each point represents the measured Sa for a given downskin parameter set and core condition.

Although many of the lowest Sa values occurred within the 20–30 J·mm^{-3} range, no clear or monotonic relationship was observed between Sa and VED. Low roughness values were achieved over a relatively broad VED range, indicating that downskin surface quality is influenced by factors beyond bulk energy input alone. Consequently, VED alone was not a reliable predictor of downskin Sa for the parameter combinations evaluated in this study.

3.2.2.1.2 Effect of Core Parameters

Among the three core conditions evaluated, 285-11-P5.1 produced both the lowest average downskin Sa (38.2 µm) and the lowest minimum Sa value (31.5 µm when combined with D6). In contrast, both the 285-12-1 and 285-11-P4 core conditions exhibited higher average Sa than 285-11-P5.1, while 285-11-P4 also showed greater variability across the evaluated downskin parameter sets. The superior performance of 285-11-P5.1 may be related to its combination of reduced energy input and relatively tight hatch spacing, which promote more stable thermal conditions during downskin formation.

3.2.2.1.3 Comparison to Literature Expectations for Downskin Roughness Behavior

The observed trends are consistent with the established understanding of overhang surface formation in L-PBF. Multiple studies have shown that downskin surface quality exhibits weak correlation with bulk energy metrics such as VED and is instead dominated by melt pool stability, local wetting behavior, and heat dissipation into the surrounding powder bed [16]. In overhanging regions, limited thermal conduction and reduced mechanical support make surface formation highly sensitive to scan speed, power density, and track overlap. Excessive local energy input promotes melt pool enlargement, sagging, and dross formation, whereas insufficient energy leads to incomplete wetting, discontinuous tracks, and balling [16–19].

The present results align with these findings, as low Sa values were achieved across a range of VED values and higher VED did not consistently yield smoother downskin surfaces. Many of the lowest downskin roughness values were observed at VED values between approximately 20 and 30 $J \cdot mm^{-3}$, although satisfactory surface quality was also achieved outside this range. This observation is broadly consistent with literature reports describing a balance between continuous track formation and melt pool stability for overhanging geometries [17]. Additionally, the improved downskin performance observed for the 285-11-P5.1 condition may be partially attributable to its relatively tight hatch spacing (0.11 mm), which increases scan-track overlap and can improve melt pool continuity and surface quality on inclined surfaces [16, 17]. Overall, the downskin roughness behavior measured here is in good agreement with established L-PBF processing trends for overhangs and downskin surfaces.

3.2.3 Selection of Core and Downskin Parameters for Hardware Production

Among the evaluated core parameter conditions, 285-11-P5.1 exhibited the most favorable overall balance of density, microstructure, surface quality, and process robustness, characterized by:

- Low porosity (<0.04% in both the as-built and HIP-ed conditions)
- Higher recrystallization response and more uniform grain structure
- Moderate energy input (VED = 61.11 J/mm^3)
- Improved downskin and top surface quality

In addition to favorable porosity and microstructural characteristics, parameter set 285-11-P5.1 produced the lowest average downskin Sa (38.2 μm) among the evaluated core conditions and demonstrated consistently good performance across the downskin parameter matrix. The improved downskin behavior may be attributable to the combination of relatively low energy input and tight hatch spacing (0.11 mm), which can promote stable melt pool behavior and improve scan-track overlap. Among the evaluated downskin conditions, D5/D11 consistently produced low Sa and demonstrated good repeatability through the duplicate build. Although D6 produced the lowest individual Sa value, its performance exhibited greater variability across the evaluated core conditions. Consequently, the combination of core parameter set 285-11-P5.1 and downskin parameter D5 was selected for demonstration hardware fabrication. The duplicate D11 build provided additional confirmation of the repeatability of this downskin condition.

Based on the combined porosity (Figure 6), microstructural characterization, downskin Sa (Figures 8 and 9), and process robustness results, 285-11-P5.1 was selected as the baseline core processing condition for hardware production, with D5 selected as the corresponding downskin parameter set. The duplicate D11 build provided additional verification of process repeatability.

3.3 Post-Processing Heat Treatment and Microstructure Evolution

3.3.1 As-Deposited Microstructure

The as-built microstructure of L-PBF NASA HR-2 was characterized to evaluate the influence of process parameters on melt pool geometry, epitaxial grain growth, and consolidation behavior. In the as-built condition, the microstructure exhibits the characteristic arc-shaped melt pools associated with layer-by-layer solidification during L-PBF processing. XZ cross-sections parallel to the build direction reveal overlapping melt pools resulting from repeated thermal cycling during deposition.

Across all evaluated conditions, melt pools were continuous and well defined, with smooth boundaries and minimal evidence of keyholing or significant lack-of-fusion defects, indicating stable processing and excellent printability throughout the parameter space investigated. Representative optical micrographs illustrating the influence of VED on melt pool morphology are shown in Figure 10. The high-VED condition (285-11-P4, 67.5 J/mm³) exhibits deep,

continuous melt pools with extensive epitaxial grain growth across multiple deposited layers. The medium-VED condition (285-12-1, 58.2 J/mm³) exhibits well-defined melt pools with partially continuous epitaxial growth and limited formation of fine equiaxed grains. In contrast, the low-VED condition (285-12-5, 45.7 J/mm³) produces comparatively shallow melt pools with disrupted epitaxial growth and increased formation of fine equiaxed grains within the melt pool interior.

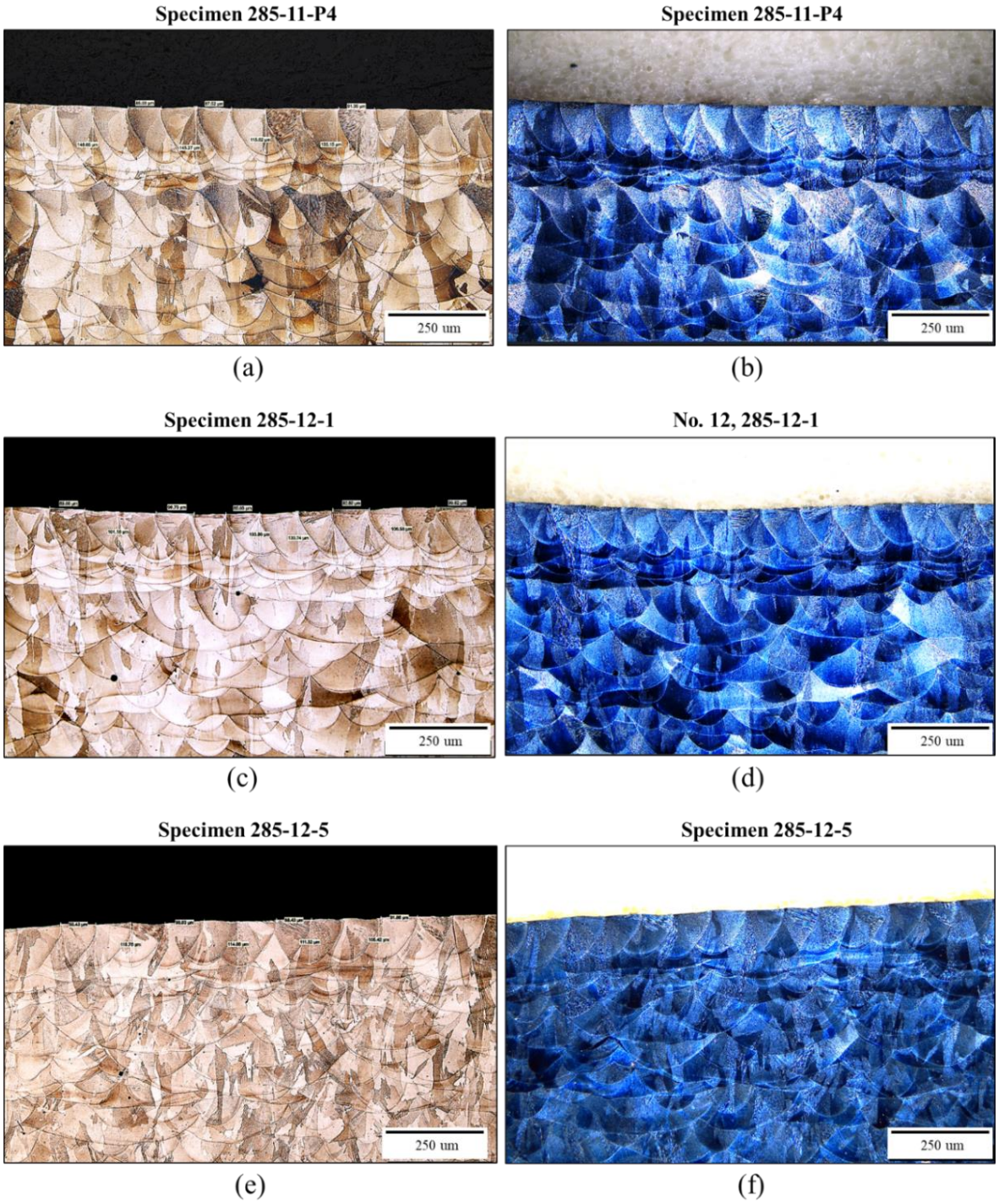

Figure 10. Effect of VED on melt pool morphology and grain structure development in as-built L-PBF NASA HR-2. (a, b) High VED (285-11-P4, 67.5 J/mm³): deep, continuous melt pools with extensive epitaxial growth. (c, d) Medium VED (285-12-1, 58.2 J/mm³): well-defined melt pools with partially continuous epitaxial growth. (e, f) Low VED (285-12-5, 45.7 J/mm³): shallow melt pools with disrupted epitaxial growth and formation of fine equiaxed grains within the melt pool interior.

Table 7 confirms that melt pool depth increases with increasing VED, from 111.3 µm (low VED) to 133.7 µm (medium VED) and 148.7 µm (high VED). These variations in melt pool geometry strongly influence epitaxial growth continuity and the subsequent recrystallization response during post-processing. Higher VED promotes deeper melt pools and more continuous epitaxial grain growth, which may facilitate greater in-situ thermal recovery and reduce the amount of stored deformation energy retained in the as-built microstructure. Conversely, lower VED conditions exhibit finer microstructural features and a greater propensity for recrystallization during subsequent post-processing.

Table 7. Influence of VED on melt pool geometry and as-built microstructure in L-PBF NASA HR-2.

VED Category	Sample ID	VED (J/mm³)	Melt Pool Depth (µm)	Epitaxial Growth Continuity	Relative Stored Energy	Relative Recrystallization Potential
High	285-11-P4	67.5	148.7	High	Low	Low
Medium	285-12-1	58.2	133.7	Moderate	Moderate	Moderate
Low	285-12-5	45.7	111.3	Low	High	High

Note: Relative stored energy and recrystallization potential are inferred from the observed melt pool morphology and recrystallization behavior following HIP and were not directly measured.

3.3.2 Post-Processing Heat Treatment

Rapid thermal cycling during L-PBF generates substantial residual stress, microstructural heterogeneity, elemental segregation, and non-equilibrium phase distributions. Consequently, post-processing heat treatments are required to reduce residual stress, minimize residual porosity, homogenize elemental segregation, and establish a stable microstructure suitable for mechanical property evaluation.

For L-PBF NASA HR-2, the standard post-processing sequence consisted of stress relief, HIP, solution annealing, and two-step aging:

- Stress relief: 1,950 °F for 1.5 h in vacuum followed by slow furnace cooling to reduce residual stress prior to removal from the build plate.

- HIP: 2,125 °F / 15 ksi / 3 h in argon (Ar) to close internal porosity, reduce chemical segregation, and promote extensive recrystallization.
- Solution annealing: 2,050 °F for 1 h in vacuum followed by Ar quenching to dissolve existing precipitates, particularly η phase, and homogenize the matrix.
- Two-step aging: 1325 °F for 16 h followed by 1150 °F for 16 h in vacuum to precipitate and coarsen the strengthening γ′ phase.

This heat-treatment sequence produces a fine equiaxed microstructure with low residual porosity and reduced residual stress, providing a uniform starting condition for mechanical property evaluation. Stress relief and HIP play key roles in controlling recrystallization and establishing final microstructural uniformity.

3.3.3 Microstructure Evolution after Stress Relief and Hot Isostatic Pressing (HIP)

Stress relief reduces residual strain energy and mitigates part distortion through thermally activated diffusion from high-stress to low-stress regions [20]. For L-PBF NASA HR-2, stress relief at 1,950 °F for 1.5 h initiates recovery and partial recrystallization [21–24]. Subsequent HIP at 2,125 °F / 15 ksi / 3 h effectively closes internal porosity, reduces elemental segregation, and promotes extensive recrystallization. The directional as-built microstructure transforms into a fine equiaxed grain structure, significantly reducing microstructural anisotropy and improving structural uniformity.

Figure 11 presents representative XZ-plane microstructures after HIP for six conditions spanning the evaluated hatch-spacing and VED ranges. All conditions exhibit extensive recrystallization and fine equiaxed grains, indicating that HIP effectively eliminates the directional solidification features characteristic of the as-built condition. Grain size decreases slightly with decreasing VED, which is consistent with the greater recrystallization driving force associated with the finer and less continuous as-built microstructures observed at lower VED.

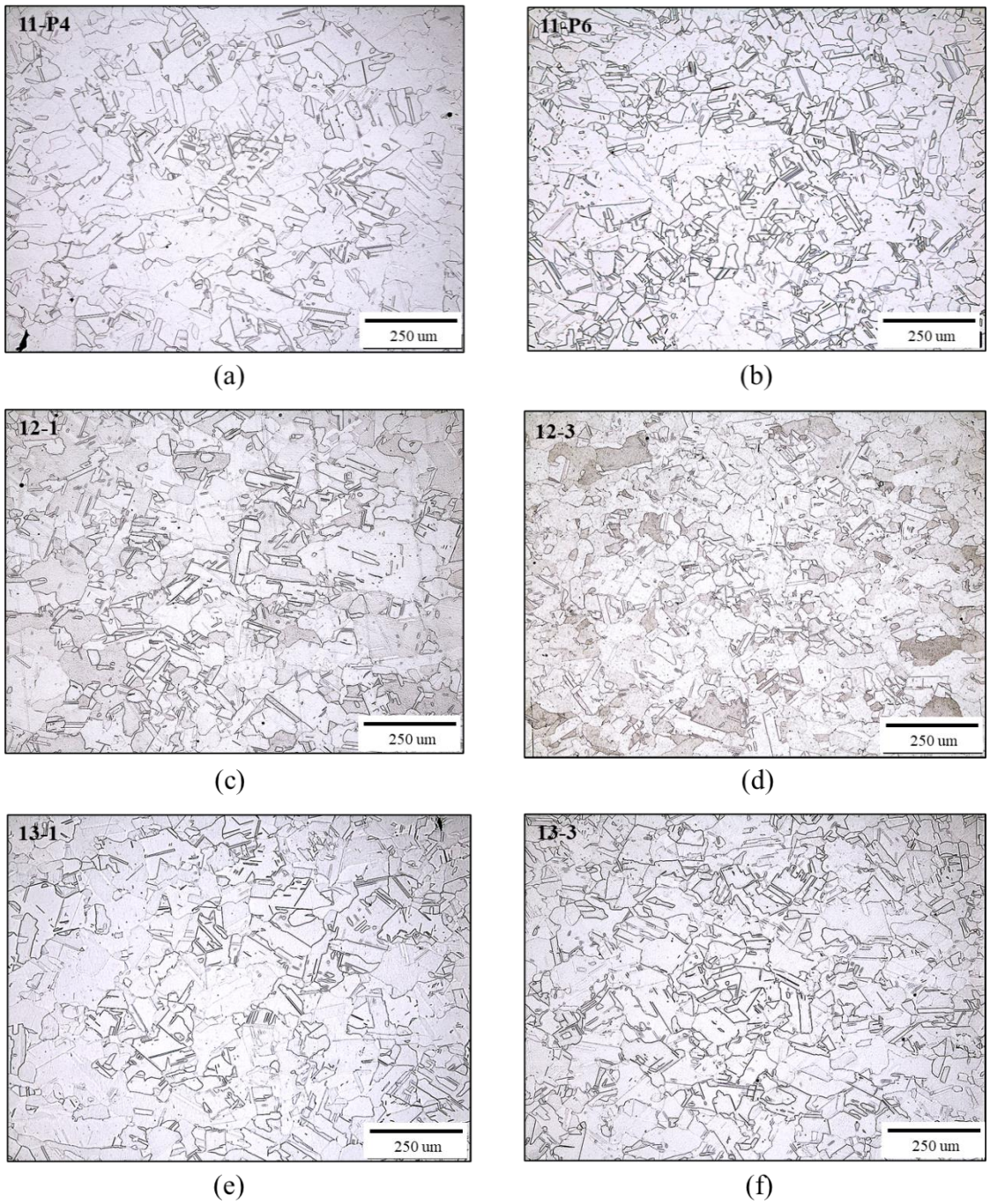

Figure 11. XZ-plane microstructures of L-PBF NASA HR-2 after HIP at 2,125 °F / 15 ksi / 3 h for representative conditions spanning hatch spacing and VED ranges. (a–b) 0.11 mm, (c–d) 0.12 mm, and (e–f) 0.13 mm hatch spacing. Across all conditions (45–67 J/mm³), HIP produces a fully recrystallized, fine equiaxed grain structure. Minor grain size variations are consistent with differences in as-built melt pool morphology and recrystallization response.

Extensive recrystallization is important for minimizing mechanical anisotropy in L-PBF materials. Previous studies on L-PBF Ni-based superalloys have shown that incomplete recrystallization and retained columnar grain structures can strongly influence tensile anisotropy and grain-boundary-controlled deformation behavior [13, 14, 25].

Surface quality was also considered during parameter selection for tensile specimens and demonstration hardware. Smaller hatch spacing and lower VED generally improved downskin surface finish; however, excessive reductions in VED increased porosity sensitivity. Considering porosity, recrystallization response, surface quality, grain structure uniformity, and processing efficiency, parameter set 285-11-P6 was selected as the preferred condition for fabrication of mechanical test specimens and demonstration hardware. This parameter set provided a favorable balance between near-full density, consistent microstructural response after HIP, acceptable surface finish, and robust process stability.

3.4 Tensile Properties in Ambient Air

3.4.1 Effect of Aging Treatment on Tensile Properties of L-PBF NASA HR-2

The tensile properties of L-PBF NASA HR-2 are strongly influenced by the combination of primary (first-step) and secondary (second-step) aging temperatures. Table 8 summarizes the tensile properties obtained under various single-step and two-step aging conditions, while Figure 12 illustrates the corresponding trends in yield strength (YS), ultimate tensile strength (UTS), and fracture elongation. The results indicate that primary aging temperature is the dominant factor governing the strength–ductility balance, whereas secondary aging between 1150–1200 °F produces comparatively minor changes.

Table 8. Summary of tensile properties of L-PBF NASA HR-2 under various aging treatments. Tensile properties for each condition are reported as the mean of three independent samples.

Material	Aging Treatment Schedule	Aging condition ID	YS (ksi)	UTS (ksi)	Fracture Elongation (%)	UTS/YS Ratio	Strain hardening exponent (n)
L-PBF NASA HR-2	1325 °F/16h	1	97.43	173.07	32.92	1.78	0.247
	1325 °F/16h + 1150 °F/16h	2	105.75	179.63	29.28	1.70	0.231
	1300 °F/16h + 1150 °F/16h	3	93.79	173.91	33.99	1.85	0.264
	1300 °F/16h + 1200 °F/16h	4	94.29	173.76	32.18	1.84	0.263
	1275 °F/16h + 1150 °F/16h	5	88.99	168.19	36.73	1.89	0.277
	1275 °F/16h + 1200 °F/16h	6	89.65	169.83	34.15	1.89	0.278

Figure 12 summarizes the influence of aging treatment on the tensile behavior of L-PBF NASA HR-2. Figure 12(a) presents the variation in YS, UTS, and fracture elongation with aging condition, while Figure 12(b) illustrates the corresponding strength-ductility tradeoff. The dashed line indicates the 95 ksi minimum yield strength requirement. Increasing primary aging temperature increases strength while reducing ductility, whereas secondary aging between 1150–1200 °F produces comparatively minor effects.

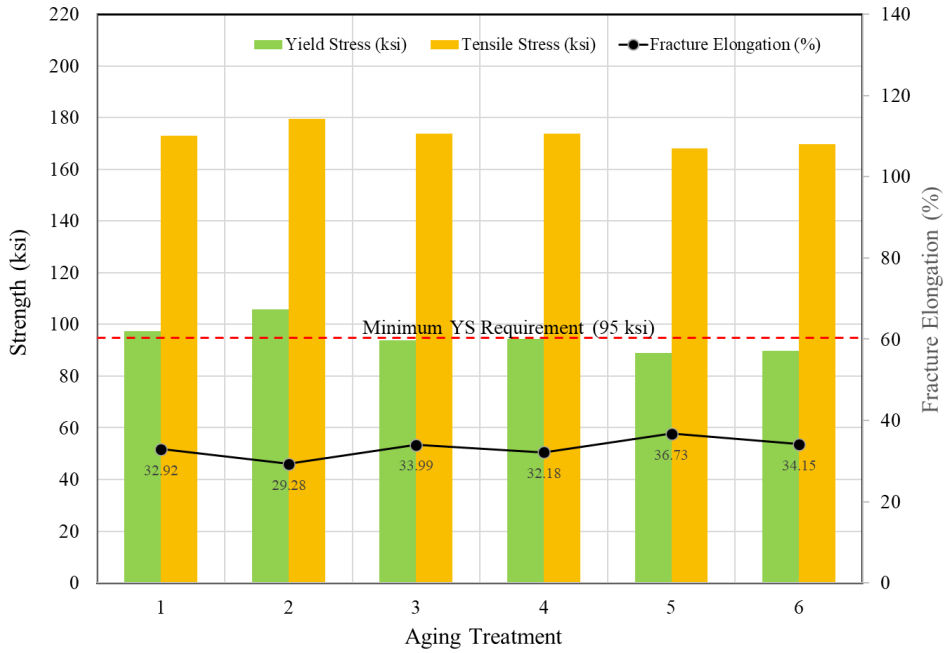

(a)

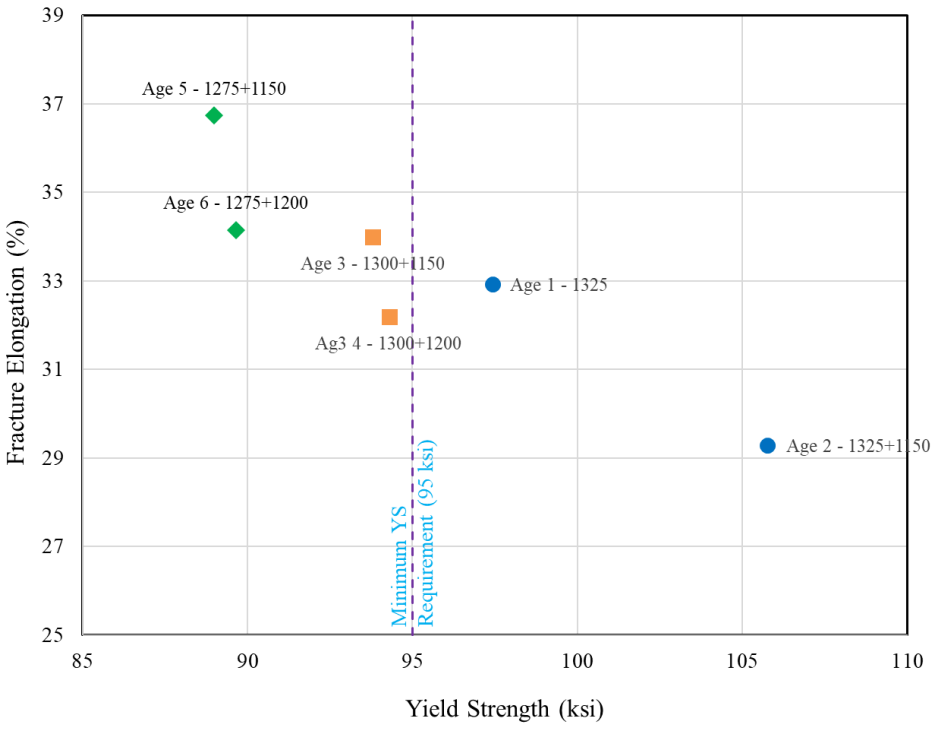

(b)

Figure 12. Effect of aging treatment on tensile properties of L-PBF NASA HR-2. (a) Yield strength, ultimate tensile strength, and fracture elongation as a function of aging condition. The dashed line indicates the 95 ksi minimum yield strength requirement. (b) Strength-ductility property map showing fracture elongation as a function of yield strength for the various aging conditions. The dashed line indicates the minimum yield strength requirement.

A single-step aging treatment at 1325 °F for 16 h yields a balanced response, with a YS of 97 ksi, UTS of 173 ksi, and fracture elongation of 33%. Addition of a secondary aging step at 1150 °F increases the YS and UTS to approximately 106 ksi and 180 ksi, respectively, indicating additional precipitation strengthening. However, elongation decreases to ~29%, suggesting reduced matrix plasticity associated with further precipitate evolution.

Reducing the primary aging temperature from 1325 °F to 1300 °F or 1275 °F decreases both YS and UTS while improving elongation and strain-hardening capacity. Two-step aging treatments with 1275–1300 °F primary aging produce UTS values near 170 ksi and fracture elongations exceeding 33%, indicating an improved balance of strength and ductility. The higher strain-hardening exponents ($n \approx 0.26$–0.28) and larger UTS/YS ratios (≈1.84–1.89) further indicate enhanced work-hardening capability and a more gradual transition from yielding to necking. These results suggest that lower primary aging temperatures produce a precipitate distribution more favorable for sustained plastic deformation.

In contrast, increasing the secondary aging temperature from 1150 °F to 1200 °F produces only minor changes in tensile behavior. For example, specimens aged at 1300 °F/16 h + 1150 °F/16 h and 1300 °F/16 h + 1200 °F/16 h exhibit nearly identical YS (93.8 vs. 94.3 ksi), UTS (173.9 vs. 173.8 ksi), and strain-hardening exponent ($n \approx 0.26$), while elongation decreases slightly (34.0% to 32.2%). Similar trends are observed for the 1275 °F primary aging condition.

For applications requiring a minimum YS of 95 ksi, primary aging temperatures of 1275–1300 °F are insufficient to consistently meet the strength requirement, even with secondary aging. Only the 1325 °F primary aging condition reliably exceeds this threshold, reaching ~105–106 ksi after secondary aging. These results highlight the fundamental tradeoff between strength and ductility in precipitation-hardened NASA HR-2. This trend is illustrated more clearly in Figure 12(b), where increasing yield strength is accompanied by a systematic reduction in fracture elongation as the primary aging temperature increases.

Overall, the results demonstrate that primary aging temperature governs the strength–ductility balance, while secondary aging provides only minor refinement with limited mechanical impact.

For applications requiring a balanced combination of strength and ductility, primary aging at 1275–1300 °F combined with secondary aging at 1150–1200 °F provides an attractive combination of UTS approaching 170 ksi, fracture elongation of approximately 34–37%, and strong work-hardening capability (UTS/YS ≈ 1.85–1.89). When a 95 ksi minimum YS requirement must be satisfied, the 1325 °F primary aging condition is preferred despite reduced ductility.

3.4.2 Temperature Dependent Tensile Properties

Temperature-dependent tensile behavior of L-PBF NASA HR-2 was evaluated using fully heat-treated specimens aged at 1325 °F/16 h + 1150 °F/16 h. Cylindrical tensile specimens were machined parallel to the build direction, as shown in Figure 2. The average tensile properties over the temperature range from −423 °F to 1300 °F are summarized in Table 9, and the corresponding trends are presented in Figure 13.

Table 9. Summary of tensile properties of L-PBF NASA HR-2 at different temperatures. Tensile properties at each temperature represent the mean of three independent samples.

Material	Aging Treatment	Test Environment & Temperature	YS (ksi)	UTS (ksi)	Fracture Elongation (%)	Strain Hardening Exponent (n)
L-PBF NASA HR-2	1325 °F/16h +1150 °F/16h	LH_2 (-423 °F)	131.07	245.02	41.24	0.299
		LN_2 (-320 °F)	120.16	221.84	38.53	0.289
		RT	102.01	174.76	32.46	0.238
		1000 °F	93.70	144.08	28.06	0.182
		1200 °F	92.56	135.26	14.24	0.165
		1300 °F	90.71	111.73	4.21	-

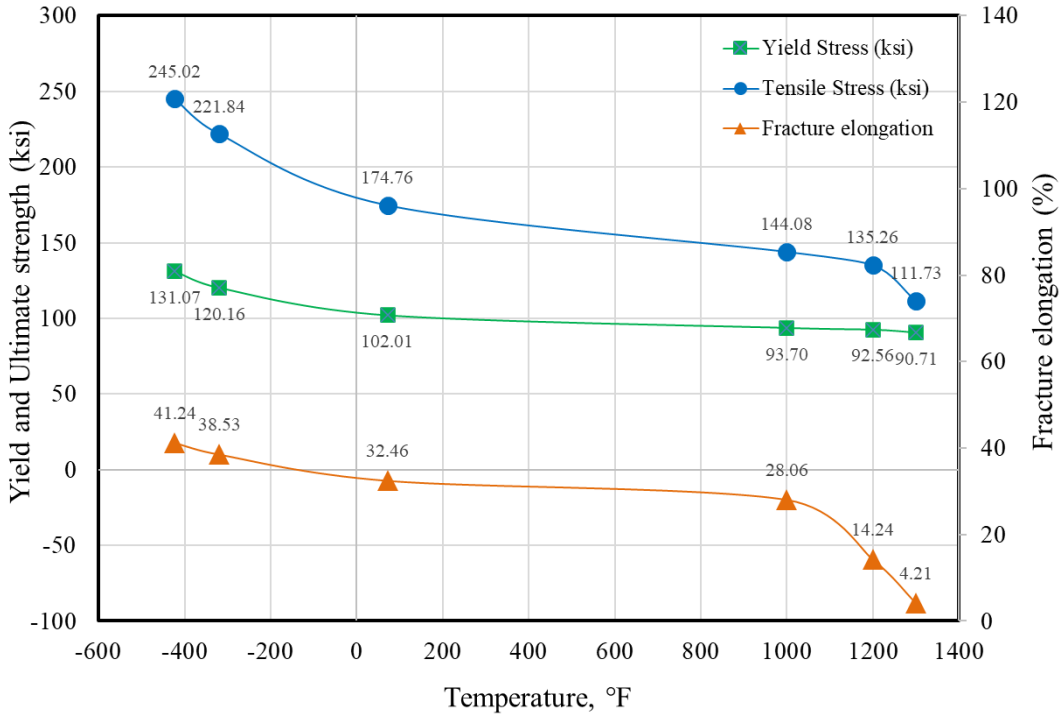

Figure 13. Temperature-dependent tensile properties from –423 °F to 1300 °F.

YS and UTS decrease monotonically with increasing temperature, from 131.07 ksi and 245.02 ksi at −423 °F to 90.71 ksi and 111.73 ksi at 1300 °F. This behavior is attributed to thermally activated dislocation motion and enhanced dynamic recovery at elevated temperatures [26].

The strain-hardening exponent (n) decreases from 0.299 at −423 °F to 0.165 at 1200 °F, indicating reduced strain-hardening capacity and a diminished ability to sustain uniform plastic deformation. A value of n was not determined at 1300 °F due to premature failure.
Fracture elongation shows a similar trend: relatively high ductility from cryogenic temperature to 1000 °F (41.24% at −423 °F to 28.06% at 1000 °F), followed by a pronounced decrease at higher temperatures (14.24% at 1200 °F and 4.21% at 1300 °F). This abrupt loss of ductility above 1200 °F indicates a transition in deformation and fracture mechanisms.

At elevated temperatures, increased atomic mobility promotes dislocation glide and dynamic recovery, reducing strain-hardening capacity, as reflected by decreasing UTS/YS ratios and strain hardening exponent (n) values. Microstructural observations at 1200 °F reveal isolated

grain-boundary cracking near fracture surfaces, suggesting a transition from predominantly transgranular fracture at lower temperatures toward increased intergranular cracking at elevated temperatures [6, 11, 27]. At these temperatures, plastic deformation can occur through a combination of dislocation slip and grain boundary sliding, particularly when grain boundaries are weaker than the grain interiors. The presence of localized intergranular fracture zones therefore suggest that grain boundary sliding became more prominent at 1,200 °F, contributing to crack formation and propagation along grain boundaries [10,11].

At cryogenic temperatures, the alloy exhibits simultaneous increases in strength and ductility, consistent with FCC deformation behavior. Enhanced strain hardening delays necking, as reflected in elevated n values and UTS/YS ratios. The enhanced tensile performance of L-PBF NASA HR-2 at cryogenic temperatures is attributed to a transition in the dominant deformation mechanism from dislocation slip at room temperature to deformation twinning at cryogenic temperatures [10,11]. Numerous deformation twins form during tensile deformation at cryogenic temperatures, acting as strong barriers to dislocation motion and thereby increasing the yield strength. The profuse formation of deformation twins also promotes additional strain hardening, delaying localized deformation and contributing to the improved fracture elongation [10,11].

Overall, L-PBF NASA HR-2 demonstrates favorable tensile performance from cryogenic to intermediate temperatures. However, the significant reduction in ductility above 1200 °F suggests that this temperature represents a practical upper limit for structural applications.

3.4.3 Tensile Deformation Behavior in Cryogenic Conditions

As shown in Table 9 and Figure 13, L-PBF NASA HR-2 exhibits strong temperature dependence, with both YS and UTS increasing from ~102 ksi and ~175 ksi at room temperature to ~131 ksi and ~245 ksi in liquid hydrogen (LH_2). Fracture elongation also increases from ~32% at room temperature to >41% in LH_2, indicating simultaneous strengthening and ductility improvement typical of FCC alloys at cryogenic temperatures.

The strain-hardening exponent (n) increases from 0.238 at room temperature to 0.299 in LH_2, indicating enhanced strain-hardening capacity. Serrated flow is observed in LH_2 at high strains

(~28–30%) in Figure 14 but is absent at room temperature and in liquid nitrogen (LN_2). The delayed onset of serrations indicates that plastic deformation remains relatively stable over most of the strain range, with intermittent flow instabilities occurring only at high strains.

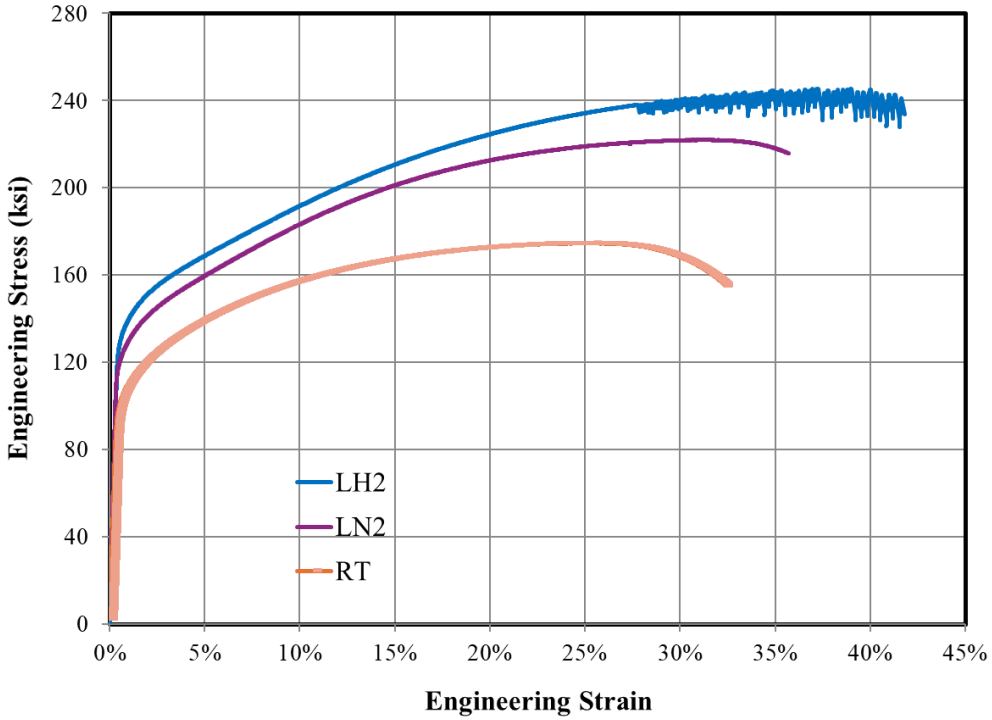

Figure 14. Engineering stress–strain curves of L-PBF HR-2 tested at −423 °F (LH_2), −320 °F (LN_2), and room temperature (RT).

The cryogenic response indicates a transition in deformation behavior with decreasing temperature. The simultaneous increase in strength, ductility, and strain hardening is consistent with suppressed cross-slip, increased planar slip, enhanced dislocation storage, and possible mechanical twinning in FCC alloys at cryogenic temperatures [11, 28–34]. These mechanisms increase the resistance to dislocation motion while maintaining substantial strain-hardening capacity, thereby delaying plastic instability and necking.

The serrated flow observed in LH_2 is consistent with athermal dislocation instabilities reported in high-strength FCC alloys at cryogenic temperatures [35, 36]. Suppressed cross-slip promotes dislocation accumulation and intermittent, avalanche-like plastic flow, producing serrations without diffusion-controlled dynamic strain aging. The moderate serration amplitude and

delayed onset (~30% strain) suggest that these instabilities have a limited effect on the overall deformation behavior.

Overall, the cryogenic response of L-PBF NASA HR-2 is characterized by increased strength, enhanced strain hardening, and retained high ductility, with localized athermal flow instabilities appearing only at high strains.

3.4.4 L-PBF NASA HR-2 and Wrought A-286 Comparison

The cryogenic tensile properties of L-PBF NASA HR-2 are compared with wrought A-286 from literature [37], as shown in Figure 15. For both alloys, strength increases with decreasing temperature, and fracture elongation improves as temperature decreases from room temperature to −320 °F. However, their ductility responses diverge at −423 °F.

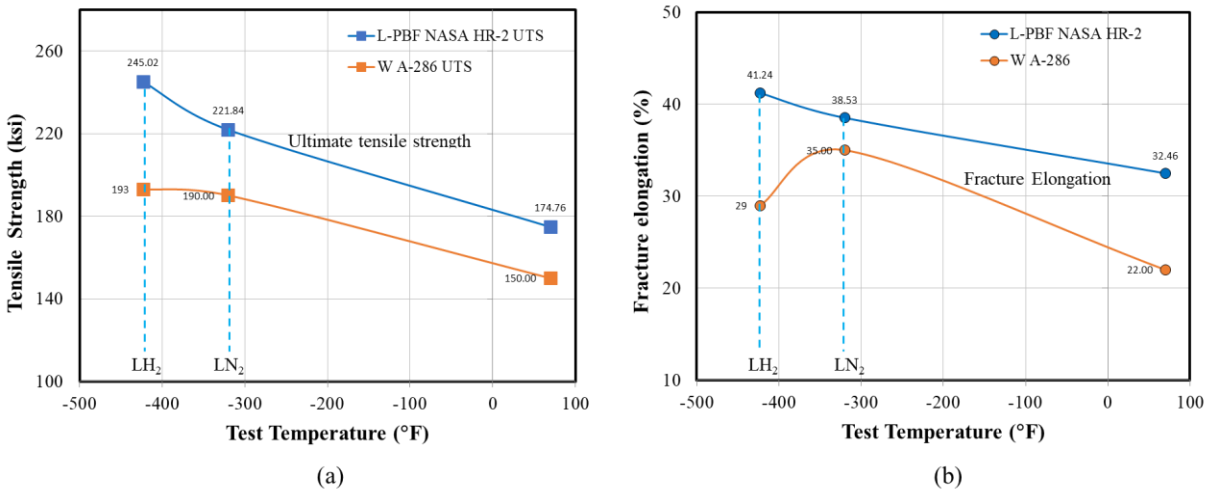

Figure 15. Cryogenic tensile properties of L-PBF NASA HR-2 compared with wrought A-286 [37]: (a) yield and tensile strengths and (b) fracture elongation.

For wrought A-286, fracture elongation increases to approximately 35% at −320 °F but decreases to ~29% at −423 °F. In contrast, L-PBF NASA HR-2 exhibits a continued increase in ductility, with fracture elongation increasing from 38.53% at −320 °F to 41.24% at −423 °F. HR-2 also exhibits substantially higher ultimate tensile strength and fracture elongation than A-286 across the evaluated cryogenic temperature range, although its yield strength is slightly lower.

Overall, L-PBF NASA HR-2 demonstrates a superior combination of strength and ductility at cryogenic temperatures compared with wrought A-286. The enhanced cryogenic response of HR-2 is attributed to increased strain hardening and improved plastic stability at low temperature, making the alloy highly promising for hydrogen-fueled liquid rocket engine applications operating under cryogenic conditions.

3.5 Tensile Properties in high Pressure Gaseous Hydrogen (GH_2) Environment

Room-temperature (RT) tensile testing in 5-ksi high-pressure GH_2 was conducted on L-PBF NASA HR-2 fabricated using the EOS M290 system to evaluate susceptibility to HEE. Results were compared with companion tests performed in laboratory air for three aging treatments spanning a range of strength levels, ductility levels, and primary/secondary aging temperatures. YS, ultimate UTS, fracture elongation, onset of necking strain, and strain hardening exponent (n) were determined using extensometer-based measurements to ensure consistent strain evaluation in both environments.

As summarized in Table 10, YS and UTS measured in 5-ksi GH_2 were slightly lower than those measured in air for all aging conditions. The reduction in YS was approximately 1–3 ksi, while UTS decreased by approximately 2–4 ksi. These differences are small and consistent across the aging conditions and do not indicate significant hydrogen-induced strength degradation. The small differences in measured properties may also be influenced by the use of different tensile-testing cells and test configurations for the air and GH_2 tests.

Table 10. Tensile properties of L-PBF NASA HR-2 tested in ambient air and 5-ksi GH_2 at room temperature. Specimens were heat treated using three aging cycles.

Aging Treatment	Environment	YS (ksi)	UTS (ksi)	Fracture Elongation (%)	Onset of necking (Engineering Strain) (%)	Strain hardening exponent (n)
Age 2: 1325 °F/16h + 1150 °F/16h	RT, Air	105.75	179.63	29.28	23.85	0.231
	RT, 5 ksi GH_2	103.00	175.80	31.41	26.08	0.238
Age 4: 1300 °F/16h + 1200 °F/16h	RT, Air	94.29	173.76	32.18	26.02	0.263
	RT, 5 ksi GH_2	91.69	170.65	34.39	29.30	0.276
Age 6: 1275 °F/16h + 1200 °F/16h	RT, Air	89.65	169.83	34.15	28.48	0.278
	RT, 5 ksi GH_2	87.93	167.51	37.24	31.61	0.292

Figure 16 compares the tensile properties measured in laboratory air and 5-ksi GH_2 for all aging conditions. Fracture elongation was maintained or slightly increased in GH_2 for all three aging conditions. For Age 2, for example, elongation increased from 29.28% in air to 31.41% in GH_2. Similar trends were observed for Age 4 and Age 6. The slightly higher elongation does not indicate a hydrogen-induced improvement in ductility; rather, it demonstrates that hydrogen exposure under the tested conditions did not cause premature fracture or loss of deformation capacity. Differences in testing cells and configurations may contribute to the observed variations.

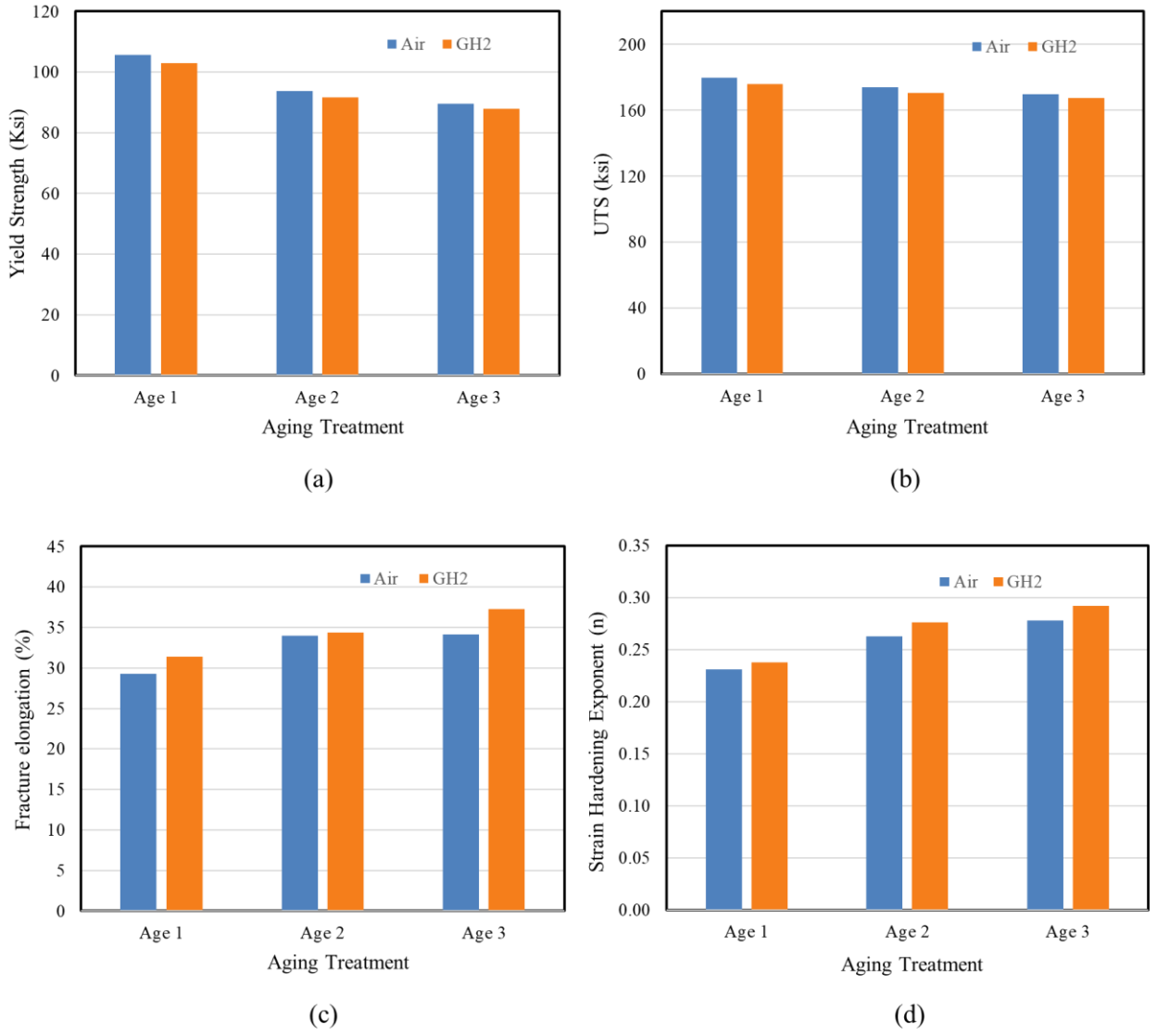

Figure 16. Comparison of tensile properties of L-PBF NASA HR-2 tested in laboratory air and 5-ksi GH_2 at room temperature for three aging conditions: (a) yield strength, (b) ultimate tensile strength (UTS), (c) fracture elongation, and (d) strain hardening exponent (n). Strength levels are comparable in both environments, while fracture elongation and strain hardening exponent are retained or slightly increased in GH_2.

The onset of necking occurred at higher strains in GH_2 for all three aging conditions.. For Age 2, the necking strain increases from 23.85% in air to 26.08% in GH_2; for Age 4, from 26.02% to 29.30%; for Age 6, from 28.48% to 31.61%. Based on the Considère criterion ($d\sigma/d\varepsilon = \sigma$) [38, 39], this behavior indicates that strain-hardening capacity is maintained or slightly increased during uniform deformation in hydrogen, delaying the onset of plastic instability.

Consistent with this trend, the strain hardening exponent (n), calculated from true stress–true strain data within the uniform deformation regime, increases slightly in GH_2 across all aging conditions ($\Delta n \approx 0.007–0.014$). Since n reflects strain hardening prior to geometric instability, the combined increase in measured n and necking strain indicates that hydrogen exposure does not adversely affect the strain-hardening behavior under the conditions examined.

Figure 17 shows representative engineering stress–strain curves for the Age 2 condition tested in laboratory air and GH_2. The curves exhibit closely matched strength and ductility, with slightly extended uniform deformation in hydrogen, consistent with delayed necking. The similarity of the engineering stress-strain curves further confirms that hydrogen exposure does not significantly alter the macroscopic tensile response.

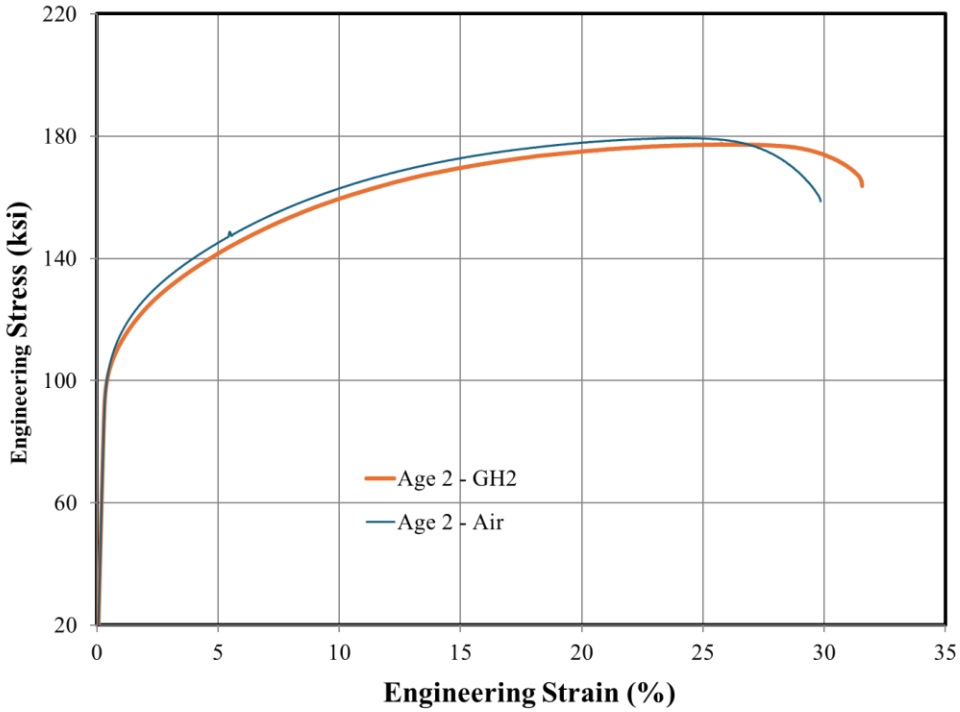

Figure 17. Representative engineering stress–strain curves for the Age 2 condition of L-PBF NASA HR-2 tested in laboratory air and 5-ksi GH_2 at room temperature, showing closely matched strength and ductility with slightly extended uniform deformation in GH_2.

Overall, L-PBF NASA HR-2 demonstrates stable and repeatable tensile behavior in 5-ksi GH_2, with no evidence of hydrogen-induced embrittlement under the conditions evaluated. Mechanical properties remain largely unchanged, fracture ductility is retained, and uniform deformation

extends to higher strains in hydrogen. Considering the small magnitude of the air-to-GH_2 differences and the use of different testing configurations, the results indicate no evidence of significant hydrogen-induced tensile embrittlement under the 5-ksi GH_2 conditions evaluated.

3.5.1 Localized Surface Cracking in Gaseous Hydrogen (GH_2)

Tensile-tested specimens exposed to 5-ksi GH_2 exhibit localized surface cracking along the gauge section, as shown in Figure 18. The cracks are shallow, discontinuous, and appear to originate from isolated surface features or microstructural heterogeneities rather than forming continuous or through-thickness fracture paths.

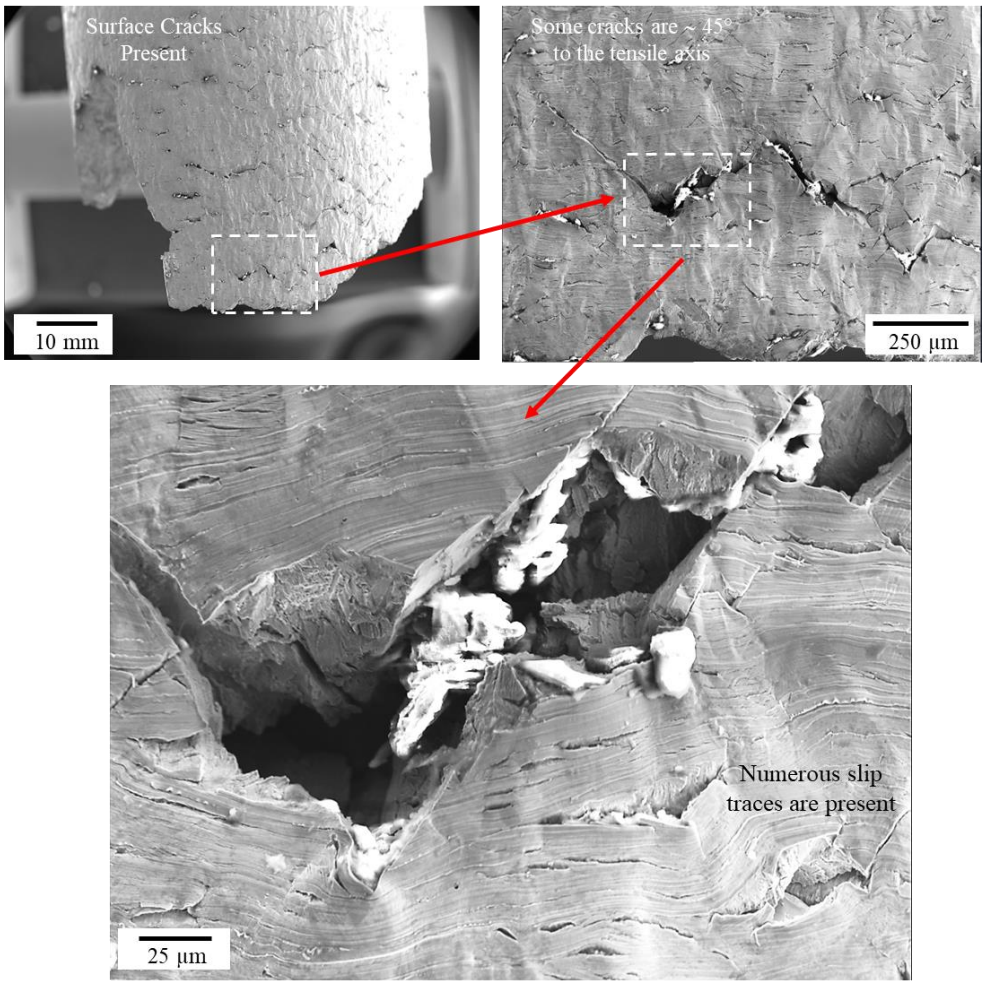

Figure 18. Surface cracking observed along the gauge section of L-PBF NASA HR-2 following tensile testing in 5-ksi GH_2. Cracks are oriented approximately 45° to the tensile axis, consistent with maximum resolved shear stress under uniaxial loading. Cracked regions exhibit extensive slip traces and plastic deformation features.

The cracked regions exhibited extensive slip traces and well-developed plastic deformation features, indicating significant dislocation activity prior to failure. Several cracks were oriented approximately 45° to the tensile axis, consistent with localized shear deformation under uniaxial loading. The coexistence of surface cracking and intense slip activity suggests that the observed damage developed concurrently with plastic deformation rather than through a predominantly brittle fracture process. Although the operative hydrogen-assisted cracking mechanism cannot be directly established from these observations, the morphology is consistent with deformation-controlled crack initiation and limited crack growth.

Despite the localized surface cracking, tensile ductility in GH_2 remains comparable to or slightly greater than that measured in air. Cross-sectional observations indicate that crack penetration is limited to approximately 100–150 μm, with no significant reduction in the effective load-bearing area. This limited penetration is consistent with the preserved fracture elongation and delayed onset of necking discussed in Section 3.5..

Overall, the observed hydrogen-induced surface damage under 5-ksi GH_2 appears to be confined primarily to the near-surface region and does not produce measurable degradation in bulk tensile response under monotonic loading.

3.5.2 Effects of Hydrogen on Fracture Behavior

Fracture surfaces were examined using SEM to assess hydrogen effects on tensile failure. Representative fractographs from a specimen tested in 5-ksi GH_2 are shown in Figure 19.

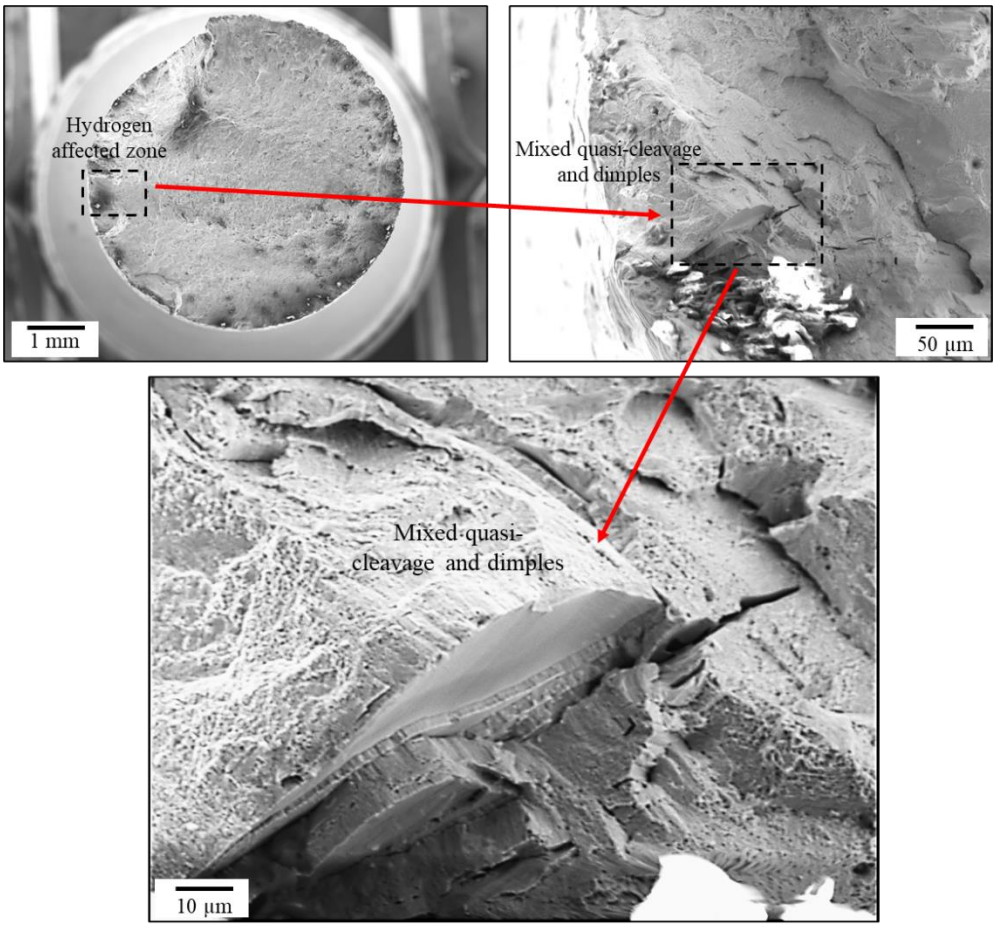

Figure 19. SEM fractography of a specimen tensile tested in 5-ksi GH_2 showing a narrow near-surface region containing mixed ductile dimple and quasi-cleavage features. The remainder of the fracture surface is dominated by ductile dimple rupture.

Hydrogen effects are confined to a narrow region near the specimen perimeter. This region contains a mixture of ductile dimples and isolated quasi-cleavage features, indicating extensive plastic deformation prior to failure. No intergranular fracture was observed, indicating that hydrogen exposure did not promote grain-boundary-dominated fracture under the conditions evaluated.

Fractographic measurements showed that the near-surface hydrogen-induced cracking region extended only approximately 100 µm into the material. This limited penetration is consistent with the shallow surface cracking observed in Section 3.5.1 and the preserved tensile ductility measured in GH_2.

3.5.3 Summary of Hydrogen Effects on Tensile Properties, Deformation, and Fracture Behavior

Overall, the fracture behavior remained predominantly ductile, with localized quasi-cleavage features confined to a shallow near-surface region. The absence of intergranular fracture and the limited depth of the affected region indicate that 5-ksi GH_2 produced only localized modifications to the fracture process without causing significant degradation of the bulk tensile fracture behavior.

Room-temperature tensile testing in 5-ksi GH_2 demonstrates that L-PBF NASA HR-2 maintains essentially unchanged bulk mechanical properties relative to laboratory air across all aging conditions. YS and UTS exhibit only minor reductions, while fracture elongation is fully retained or slightly increased. The strain-hardening exponent (n) and onset of necking also increase consistently in GH_2, indicating that strain-hardening capacity is maintained and plastic instability is delayed.

Microstructural and fractographic observations indicate that the effects of GH_2 exposure are primarily localized near the specimen surface, manifested by shallow surface cracks and a narrow region containing mixed ductile–quasi-cleavage features. Crack penetration is limited to approximately 100–150 μm, while the remainder of the fracture surface is dominated by ductile dimple rupture with no evidence of intergranular fracture.

Overall, the combined tensile, microstructural, and fractographic results indicate that 5-ksi GH_2 produces only localized near-surface modifications to the deformation and fracture behavior without measurable degradation of bulk tensile performance under monotonic loading. These results provide no evidence of significant hydrogen-induced tensile embrittlement of L-PBF NASA HR-2 under the conditions evaluated.

3.6 High Cycle Fatigue (HCF) Behavior of L-PBF HR-2 in Ambient Air

The HCF behavior of machined L-PBF HR-2 was evaluated under both tension–tension ($R = 0.1$) and fully reversed ($R = -1$) loading conditions to quantify stress amplitude sensitivity, endurance behavior, and mean stress effects. All HCF specimens were fully heat treated and

aged using a 1325 °F/16 h + 1150 °F/16 h cycle followed by final machining after heat treatment. The HCF specimens had a nominal gauge diameter of 0.25 in and were machined by turning to achieve a final surface roughness of approximately 8 µin Ra (arithmetic average roughness) or better as shown in Figure 3. The complete datasets are summarized in Tables 11 and 12, and the corresponding stress cycle (S–N) responses are shown in Figures 20–22.

Table 11. HCF results for L-PBF HR-2 under tension–tension loading at R = 0.1. Tests were conducted under maximum-stress-controlled conditions using machined (turned) specimens.

Machining condition	**Max Stress (ksi)**	**Stress Amplitude (ksi)**	**Cycles to Failure**	**Result**
Turned	80	36	10,000,000	Runout
	80	36	10,000,000	Runout
	80	36	5,173,693	Failure
	90	40.5	2,382,073	Failure
	90	40.5	2,007,808	Failure
	90	40.5	2,913,300	Failure
	95	42.75	1,208,131	Failure
	95	42.75	1,105,339	Failure
	100	45	445,594	Failure
	100	45	577,241	Failure

Table 12. HCF results for L-PBF HR-2 under fully reversed loading at R=−1. Tests were conducted under fully reversed stress-controlled conditions using machined (turned) specimens.

Machining condition	**Max Stress (ksi)**	**Stress Amplitude (ksi)**	**Cycles to Failure**	**Result**
Turned	55	55	10,000,000	Runout
	55	55	7,745,198	Failure
	60	60	5,270,458	Failure
	60	60	1,603,366	Failure
	60	60	10,000,000	Runout
	65	65	192,254	Failure
	65	65	270,832	Failure
	70	70	212,087	Failure
	75	75	162,443	Failure

3.6.1 Fatigue Response at R = 0.1 (Tension–Tension Loading)

Under R = 0.1 loading, the material exhibits a gradual transition from near-endurance behavior to finite-life fatigue with increasing maximum stress. At 80 ksi (36 ksi stress amplitude), two specimens achieved runout beyond 10^7 cycles, while one specimen failed at approximately 5.2×10^6 cycles, indicating that this stress level lies near the upper bound of the near-endurance regime.

At 90 ksi (40.5 ksi amplitude), fatigue life decreases to approximately $2.0–2.9 \times 10^6$ cycles, marking the onset of a clearly finite-life regime. With further increases in maximum stress to 95 ksi (42.5 ksi stress amplitude) and 100 ksi (45 ksi stress amplitude), fatigue life decreases to ~$1.1–1.2 \times 10^6$ cycles and ~$4.4–5.7 \times 10^5$ cycles, respectively, indicating progressively reduced fatigue resistance associated with earlier crack initiation and/or accelerated crack propagation.

As shown in Figure 20, the S–N response exhibits a continuous, monotonic decrease in fatigue life with increasing stress amplitude. Rather than a sharply defined knee, the data suggest a broad transition region between approximately 80 and 100 ksi maximum stress (36–45 ksi stress amplitude), where the probability of runout decreases progressively.

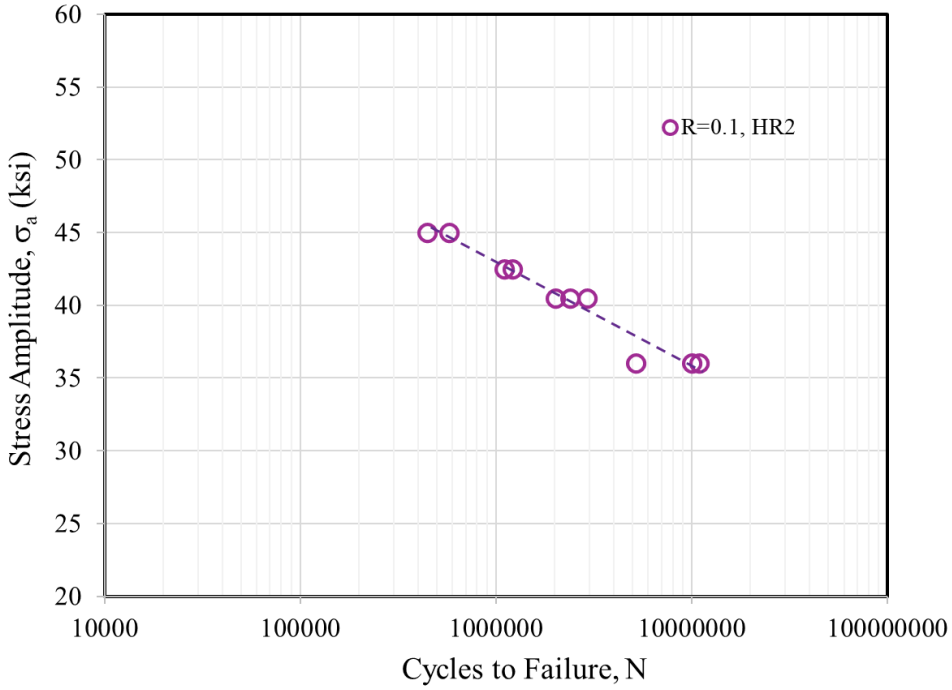

Figure 20. HCF S–N response of machined L-PBF HR-2 at $R = 0.1$. Stress amplitude is plotted versus cycles to failure on a logarithmic scale. Runout is defined as 10^7 cycles. The results show a continuous decrease in fatigue life with increasing stress amplitude.

3.6.2 Fatigue Response at R = −1 (Fully Reversed Loading)

Under fully reversed loading, HR-2 exhibits a higher apparent endurance strength and a more clearly defined near-endurance regime compared to R = 0.1 loading. At 55 ksi, one specimen achieved runout beyond 10^7 cycles while a second specimen failed at approximately 7.7×10^6 cycles, indicating that this stress level lies near the endurance threshold under fully reversed loading.

At 60 ksi, mixed behavior is observed, with both runout and failure occurring between 1.6×10^6 and 5.2×10^6 cycles, suggesting that this stress level is near the upper bound of the near-endurance regime. Increasing the stress to 65 ksi results in a sharp reduction in fatigue life to ~$2.0–2.7 \times 10^5$ cycles, defining the onset of the knee region. At 70 ksi and 75 ksi, fatigue life remains consistently in the ~$1.6–2.0 \times 10^5$ cycle range, indicating a stabilized finite-life regime at these stress levels.

As shown in Figure 21, the R = −1 response can be divided into three regimes: a near-endurance regime (55 ksi), a transition regime (60 ksi), and a finite-life regime (≥65 ksi). Compared to R = 0.1, scatter at low stress is reduced and the endurance boundary is more clearly defined.

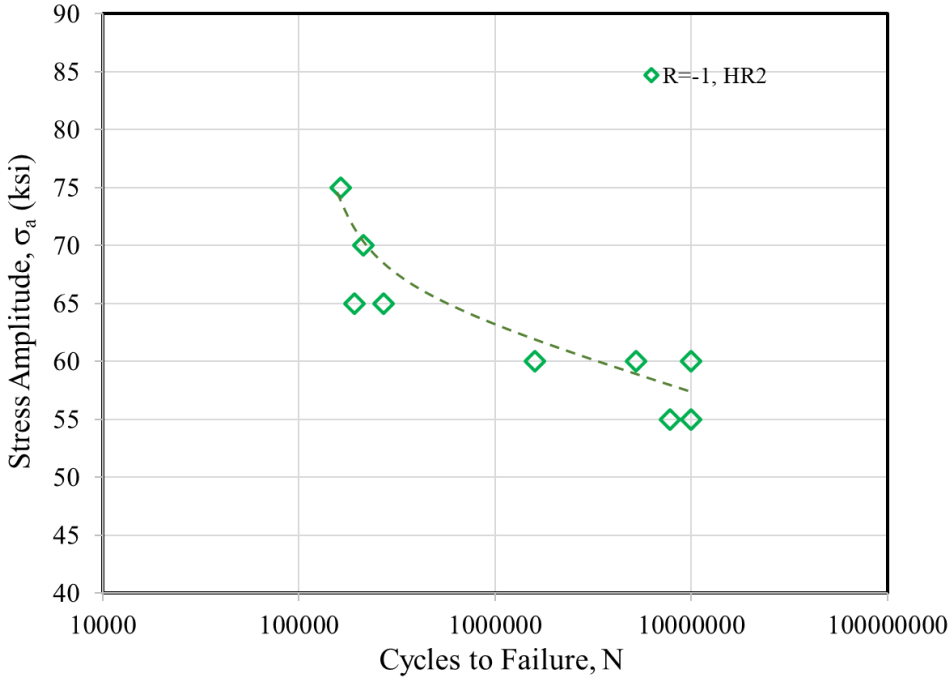

Figure 21. HCF S–N response of machined L-PBF HR-2 at R = −1 showing endurance, transition, and finite-life regimes. Stress amplitude is plotted versus cycles to failure on a logarithmic scale. Runout is defined as 10^7 cycles. The data show a well-defined near-endurance regime at 55 ksi, a transition regime at 60 ksi, and a finite-life regime at ≥65 ksi.

3.6.3 Mean Stress Effects in L-PBF HR-2

A direct comparison of the fatigue behavior of L-PBF HR-2 under R = 0.1 and R = −1 loading conditions is presented in Figure 22. The results demonstrate a pronounced sensitivity to mean stress. The apparent 10^7-cycle endurance stress amplitude decreases from approximately 55 ksi under fully reversed loading (R = −1) to approximately 36 ksi under tension–tension loading (R = 0.1), corresponding to a maximum stress of approximately 80 ksi at R = 0.1. This reduction indicates that a positive mean stress lowers the endurance capability of the alloy and promotes an earlier transition to finite-life fatigue behavior.

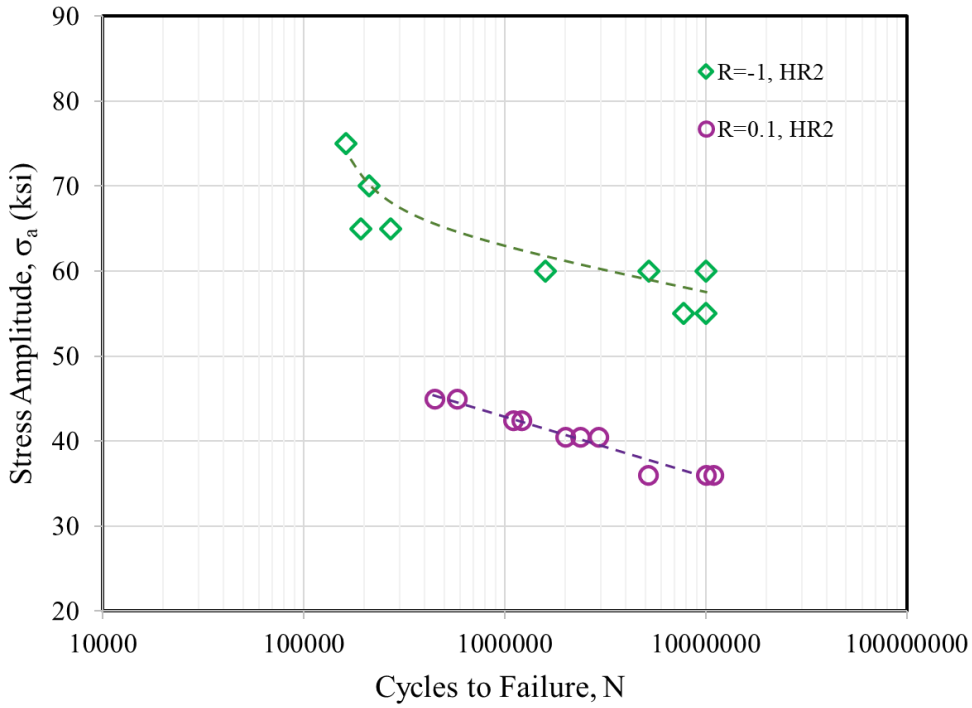

Figure 22. Comparison of the HCF behavior of machined L-PBF HR-2 under R = 0.1 and R = −1 loading conditions. The figure illustrates mean stress–induced shifts in the near-endurance, transition, and finite-life fatigue regimes, resulting in reduced fatigue resistance under positive mean stress conditions.

Positive mean stress reduces the apparent endurance threshold, whereas the fully reversed condition exhibits a more clearly defined transition from near-endurance to finite-life behavior. The observed response is consistent with slip-controlled crack initiation and early-stage short-crack growth, in which localized cyclic plasticity contributes to the transition from crack nucleation to stable propagation [40, 41].

Furthermore, the lack of evidence for defect-controlled crack initiation under the present HIP and machining conditions suggests that fatigue behavior is governed primarily by microstructurally sensitive crack initiation rather than process-induced defects, consistent with observations reported for additively manufactured Ni-based superalloys [42].

3.6.4 High-Cycle Fatigue (HCF) Behavior of L-PBF HR-2, SLM 718, and Wrought A286

The HCF behavior of L-PBF HR-2 was compared with SLM 718 and wrought A286 using data from NASA MSFC materials databases [43]. Because the datasets were generated using different specimen finishing methods (turned, low-stress ground, and turned with different Ra levels), the

comparisons should be interpreted as qualitative indicators of relative fatigue performance rather than direct material rankings. Corresponding S–N responses of L-PBF HR-2 (turned to 8 µin), SLM 718 (low-stress ground), and wrought A286 (turned to 32 µin) are shown in Figures 23 (at R = 0.1) and 24 (at R = -1).

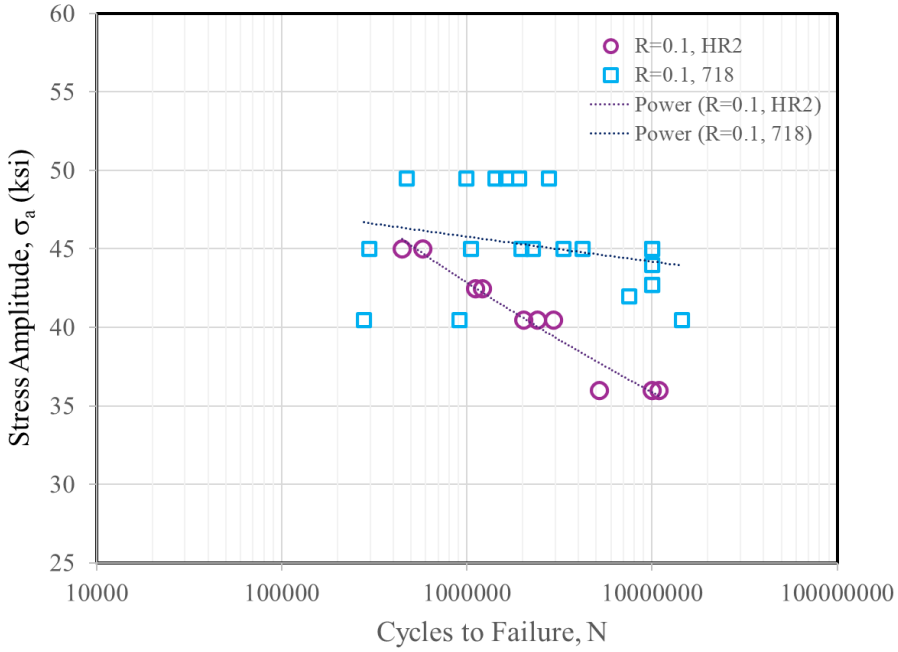

Figure 23. Comparison of the HCF S–N response of L-PBF HR-2 (turned to 8 µin), SLM 718 (low-stress ground), and wrought A286 (turned to 32 µin) at R = 0.1. Stress amplitude is plotted as a function of cycles to failure on a logarithmic scale. Runout is defined as 10^7 cycles.

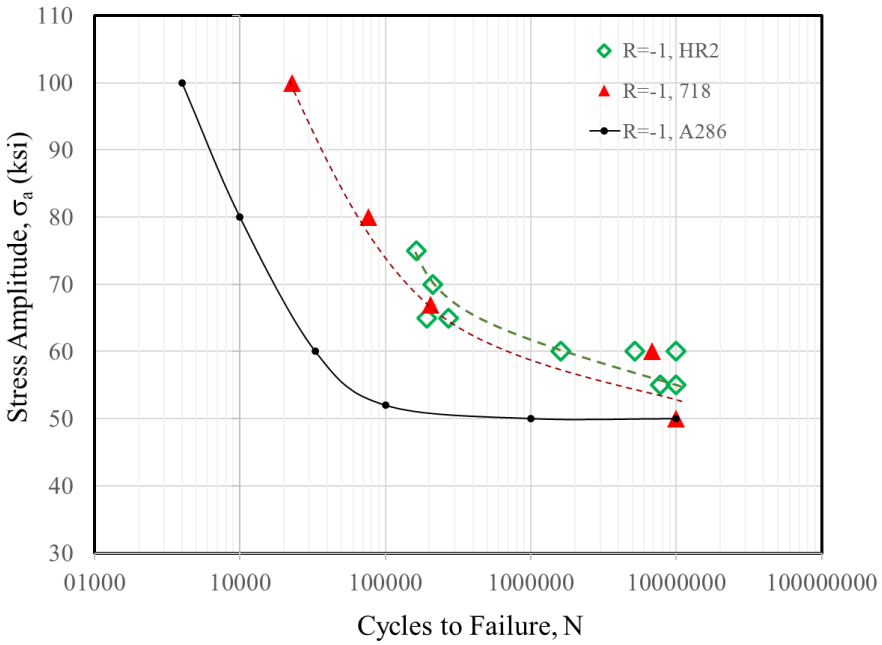

Figure 24. Comparison of the HCF S–N response of L-PBF HR-2 (turned to 8 µin), SLM 718 (low-stress ground), and wrought A286 (turned to 32 µin) at R = −1. Stress amplitude is plotted as a function of cycles to failure on a logarithmic scale. Runout is defined as 10^7 cycles and indicated by open symbols.

Under R = 0.1 loading, SLM 718 exhibits higher apparent fatigue resistance than L-PBF HR-2, consistent with its higher room-temperature strength level (~160 ksi versus ~105 ksi) as shown in Figure 23. However, SLM 718 also exhibits significant scatter in the intermediate stress regime, where both runout and failure occur at similar stress amplitudes. In contrast, L-PBF HR-2 exhibits a more uniform and predictable S–N response, with fatigue life decreasing progressively as stress amplitude increases.

Under fully reversed loading (R = −1), the differences among the three materials become more pronounced as shown in Figure 24. The fatigue response of L-PBF HR-2 approaches that of SLM 718 within the evaluated stress range and displays a relatively well-defined transition between near-endurance and finite-life behavior. -Wrought A286 exhibits the lowest fatigue resistance across the evaluated stress range.

Overall, within the available datasets, SLM 718 exhibits the highest apparent fatigue strength, HR-2 exhibits intermediate fatigue resistance with comparatively consistent behavior, and wrought A286 exhibits the lowest fatigue resistance.

Across both loading conditions, the observed fatigue behavior and fracture morphology of L-PBF HR-2 are consistent with crystallographic slip-controlled crack initiation and Stage I slip-band cracking, followed by short-crack growth governing the transition to finite life [44]. These mechanisms provide a common basis for the observed differences in scatter, apparent fatigue strength, and endurance behavior among the three alloys.

3.6.5 Fractography of High-Cycle Fatigue (HCF)-Tested Specimens

Fractographic examination was performed on all fatigue-tested specimens that failed before runout to identify crack initiation sites and characterize crack propagation mechanisms. High-cycle fatigue cracks did not initiate from typical AM defects, such as lack-of-fusion voids. In all examined specimens, the dominant crack-initiation morphology was consistent with crystallographic Stage I cracking (CSIC), in which microcracks nucleated along highly active slip planes and produced faceted initiation regions. The results are summarized in Table 13.

Table 13. HCF results for turned specimens tested at stress ratios of R = 0.1 and R = −1. Runout is defined as 10,000,000 cycles.. CSIC denotes crystallographic Stage I cracking. For R = −1 loading, fully reversed conditions apply such that $\sigma_{max} = \sigma_a$.

R-ratio	Specimen ID	Max Stress, σ_{max} (ksi)	Stress Amplitude, σ_a (ksi)	Cycles to Failure	Crack Initiation Mode
0.1	HCF26	80	36	10,000,000	Runout
	HCF27	80	36	5,173,693	CSIC
	HCF28	80	36	10,000,000	Runout
	HCF23	90	40.5	2,382,073	CSIC
	HCF24	90	40.5	2,007,808	CSIC
	HCF25	90	40.5	2,913,300	CSIC
	HCF34	95	42.75	1,208,131	CSIC
	HCF35	95	42.75	1,105,339	CSIC
	HCF36	100	45	445,594	CSIC
	HCF37	100	45	577,241	CSIC
−1	HCF32	55	55	10,000,000	Runout
	HCF33	55	55	7,745,198	CSIC
	HCF30	60	60	5,270,458	CSIC
	HCF31	60	60	1,603,366	CSIC
	HCF41	60	60	10,000,000	Runout
	HCF38	65	65	192,254	CSIC
	HCF39	65	65	270,832	CSIC
	HCF40	70	70	212,087	CSIC
	HCF42	75	75	162,443	CSIC

Fractographic examination of the L-PBF HR-2 specimens reveals a predominantly crystallographic fatigue crack growth mechanism characterized by faceted fracture surfaces and localized slip-controlled crack advance. In all examined failed specimens, crack initiation occurred at or near the specimen surface, followed by crack propagation along crystallographic slip-planes prior to final overload fracture.

Figures 25 and 26 present representative fractographic observations for specimens HCF24 and HCF30, illustrating crack initiation and propagation behavior under R = 0.1 and R = −1 loading conditions, respectively.

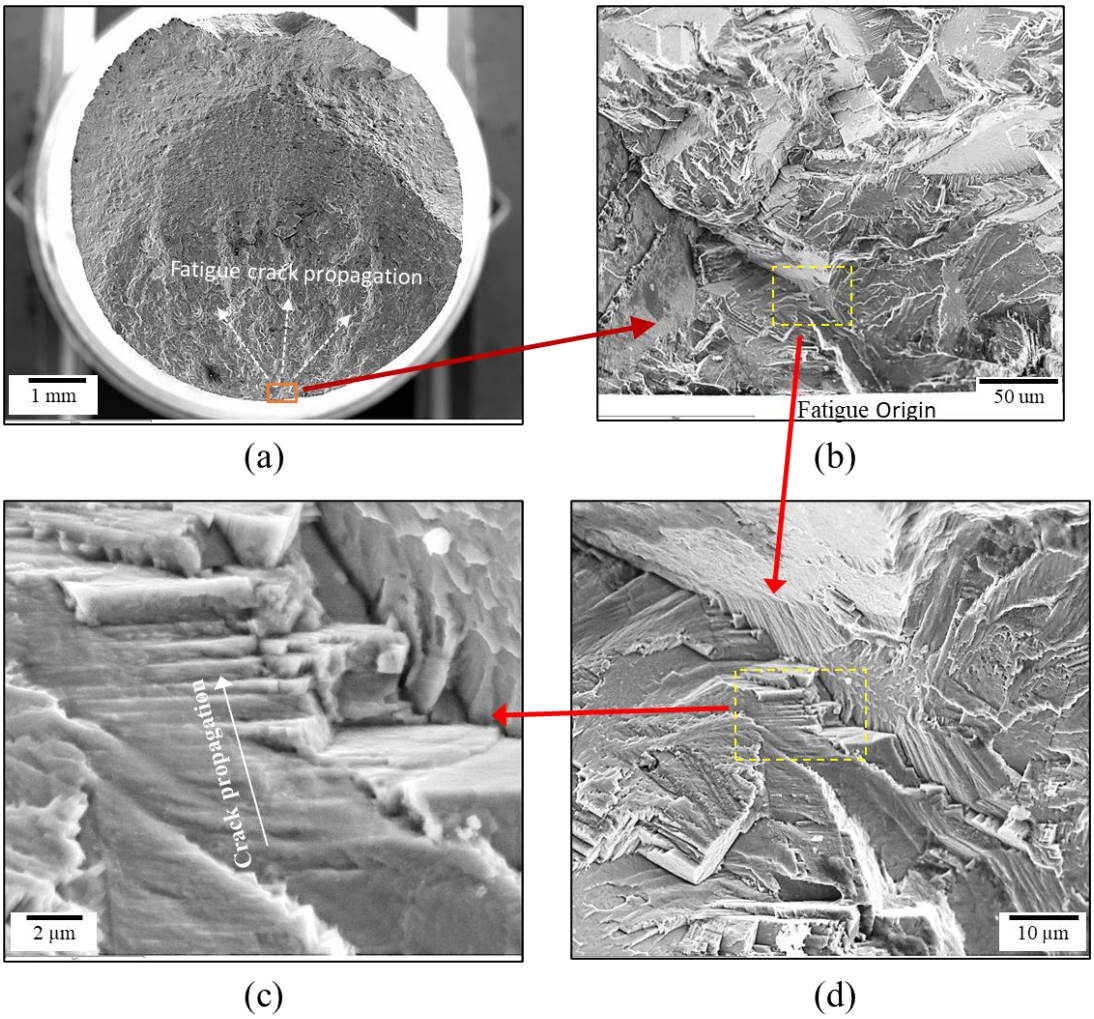

Figure 25. Fractographic analysis of specimen HCF24 following HCF testing at 90 ksi and R = 0.1. (a) Low-magnification SEM image showing the fatigue crack initiation site and propagation region relative to the final overload zone. (b–d) Higher magnification FE-SEM images of the crack origin, revealing faceted fracture morphology and slip-step features consistent with crystallographic fatigue crack growth.

Specimen HCF24 failed after approximately 2.0–2.9 million cycles under a maximum stress of 90 ksi (R = 0.1). As shown in Figure 25, the fracture surface exhibits a relatively small fatigue crack propagation region compared to the final overload zone, indicating that a significant fraction of life was consumed by stable crack growth. The crack initiated at the specimen surface and propagated inward in a highly localized manner. Higher magnification imaging reveals a faceted fracture morphology and fine slip-step features near the crack origin, consistent with crystallographically controlled fatigue crack growth.

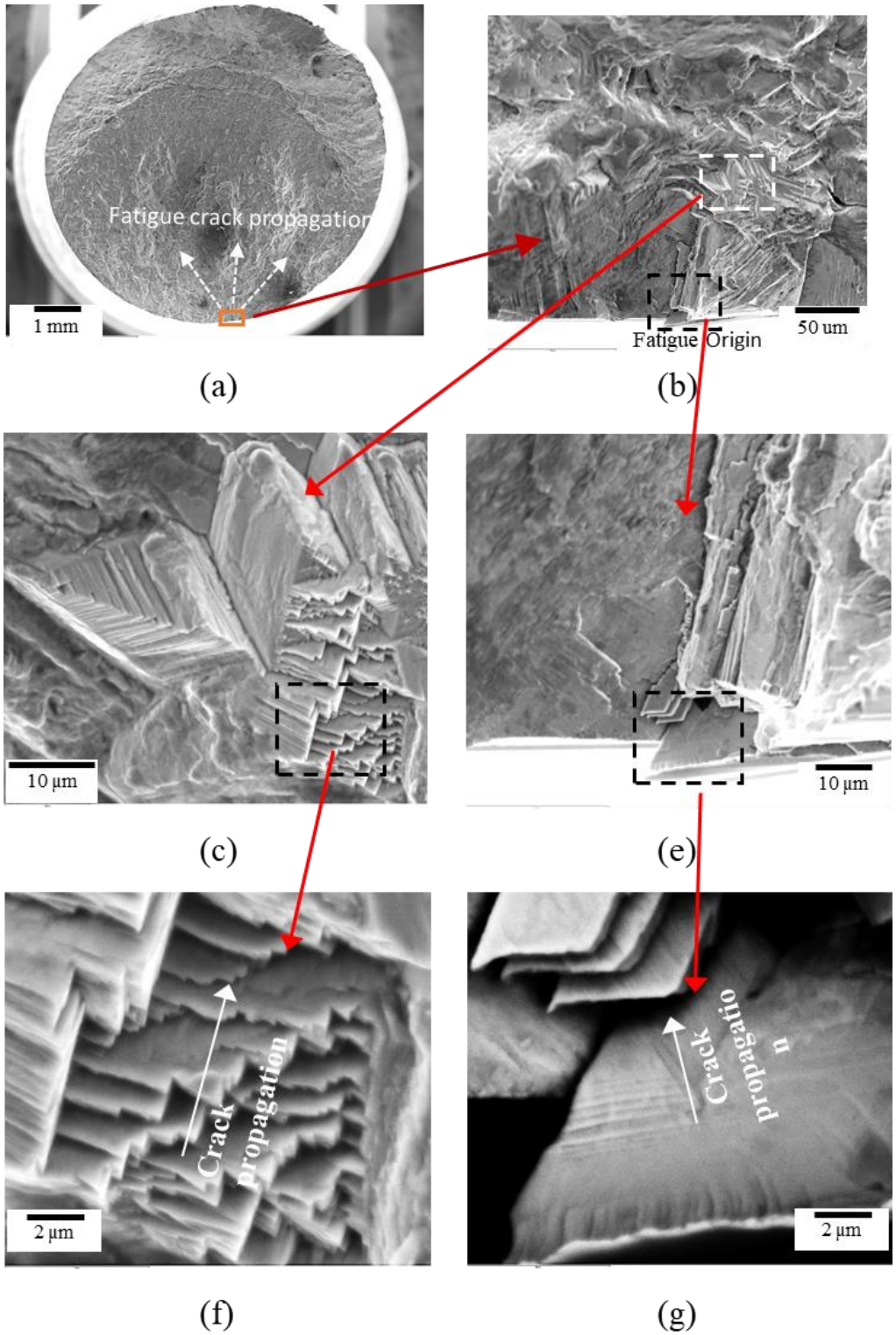

Figure 26. Fractographic analysis of L-PBF HR-2 specimen HCF30 following HCF testing at 60 ksi under R = −1 loading. (a) Low-magnification SEM image showing the fatigue crack propagation region and final overload zone. (b–f) Higher magnification FE-SEM images of the crack origin, revealing a faceted fracture morphology and localized slip activity associated with crystallographic fatigue crack growth.

Specimen HCF30 failed after approximately 5.2 million cycles under a maximum stress of 60 ksi ($R = -1$). As shown in Figure 26, the fracture surface similarly shows a well-defined fatigue crack propagation region that is small relative to the overload zone, indicating stable crack growth over most of the fatigue life. The crack initiated at or near the specimen surface and propagated along crystallographic planes in a highly localized manner, producing faceted fracture morphology consistent with slip-controlled fatigue cracking.

The observed fracture morphology across all specimens is consistent with slip-controlled crack initiation and crystallographically guided early-stage crack propagation, which are characteristic features of Stage I fatigue damage in FCC alloys and superalloys [45, 46]. The limited evidence of microvoid coalescence or secondary cracking near the crack origins indicates that fatigue damage accumulation was dominated by localized cyclic slip with minimal macroscopic plastic deformation. These observations were consistently observed across all failed specimens examined in this study.

3.7 Demonstration Hardware Fabrication

L-PBF NASA HR-2 has demonstrated excellent printability and strong resistance to HEE. Building on these capabilities, demonstration hardware was fabricated to evaluate the manufacturability of complex hydrogen-sensitive components and explore practical design limits for L-PBF processing.

These demonstration builds established the manufacturability of several key components for the RS-25 LPFTP, including a lift-off seal housing (Figure 27) and a single-piece rotor integrating the turbine wheel, pump shaft, and second-stage rotor into a monolithic structure (Figure 28). The single-piece rotor eliminates mechanical joints, improving torque transmission and overall reliability. Because the single-piece rotor component operates under high centrifugal stresses in a hydrogen environment, resistance to hydrogen embrittlement is critical for structural integrity and reliable turbopump operation.

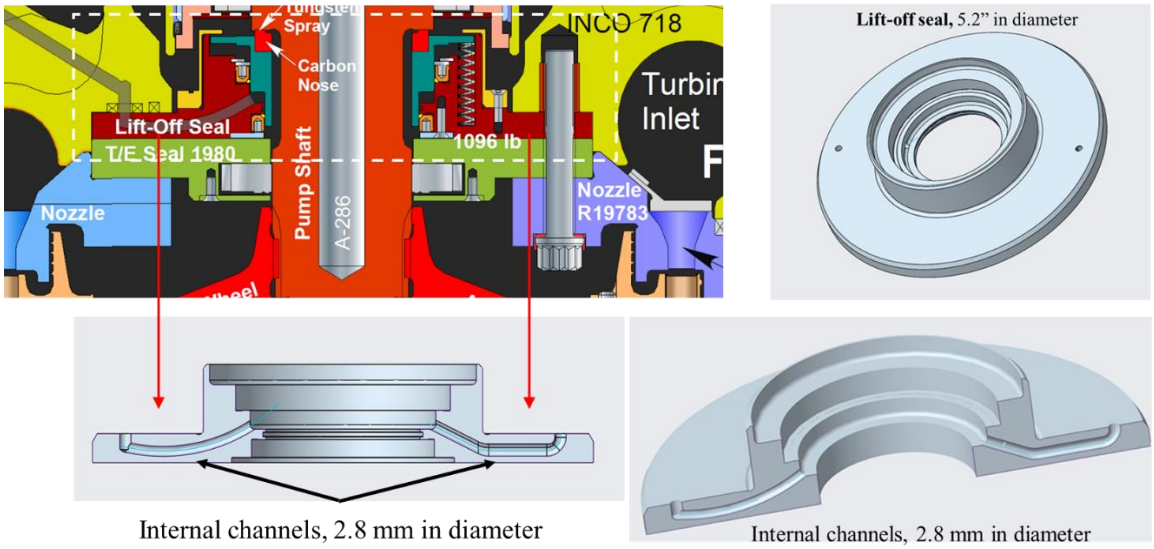

(a)

CAD Model of Lift-Off Seal Housing

Printed Lift-Off Seal Housing

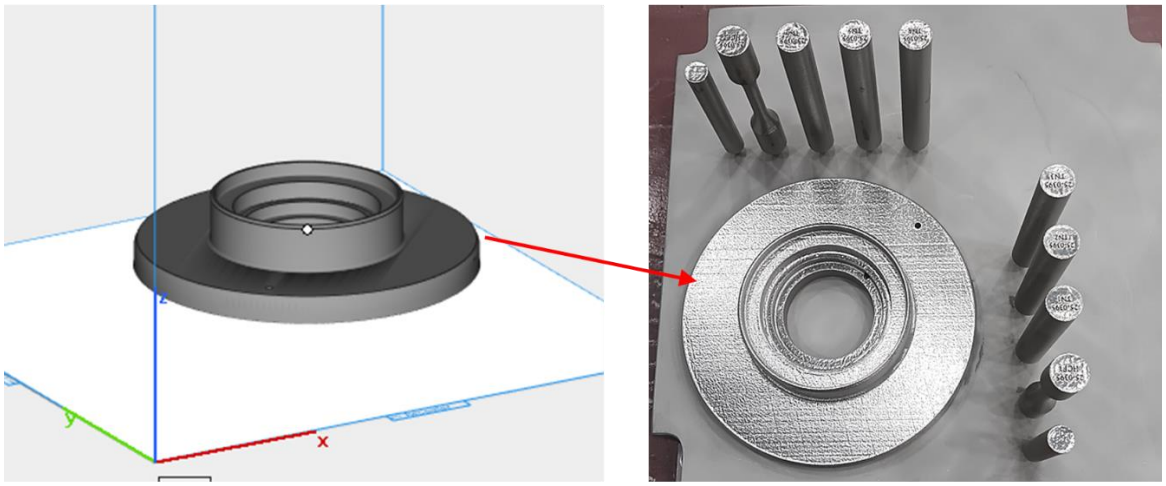

(b)

Figure 27. (a) Lift-off seal housing for the RS-25 LPFTP. (b) CAD model and successfully printed full lift-off seal housing.

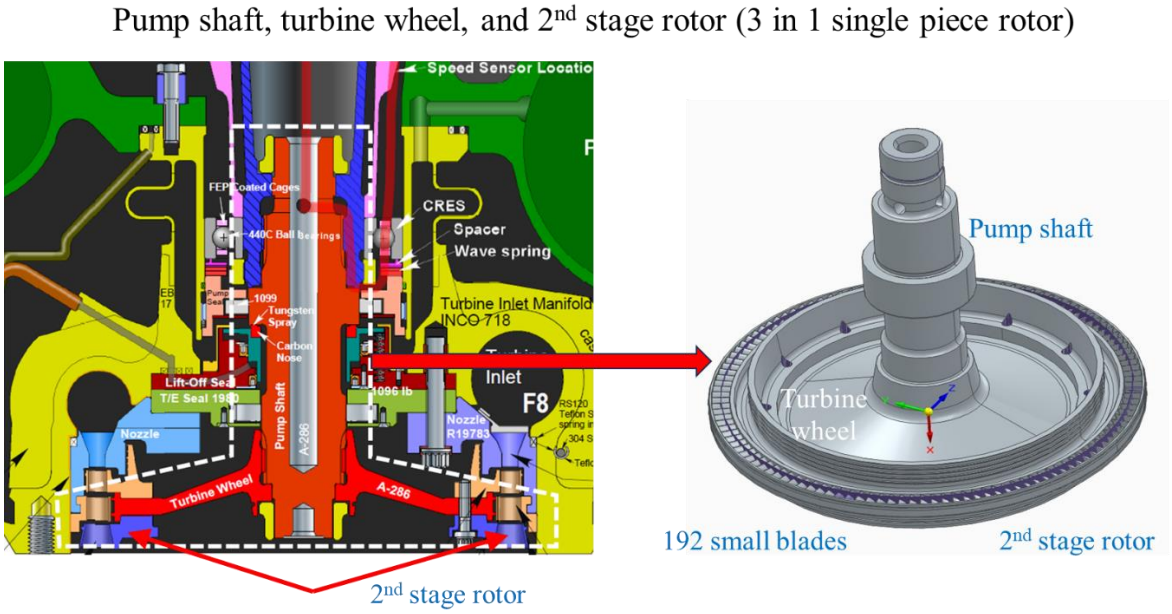

Figure 28. (a) CAD model of the single-piece rotor for the RS-25 LPFTP. (b) CAD model of a 45° rotor section illustrating support structure design and the corresponding successfully printed component.

In addition, a large mixer component for the RS-25 nozzle was successfully fabricated (Figure 29). The mixer combines hydrogen coolant streams from multiple regenerative cooling channels into a uniform flow prior to film-coolant injection, ensuring balanced thermal conditions and preventing localized overheating. Exposed to sustained mechanical and thermal loading in a hydrogen environment, the component similarly requires high resistance to hydrogen-induced embrittlement to maintain structural integrity and reusability.

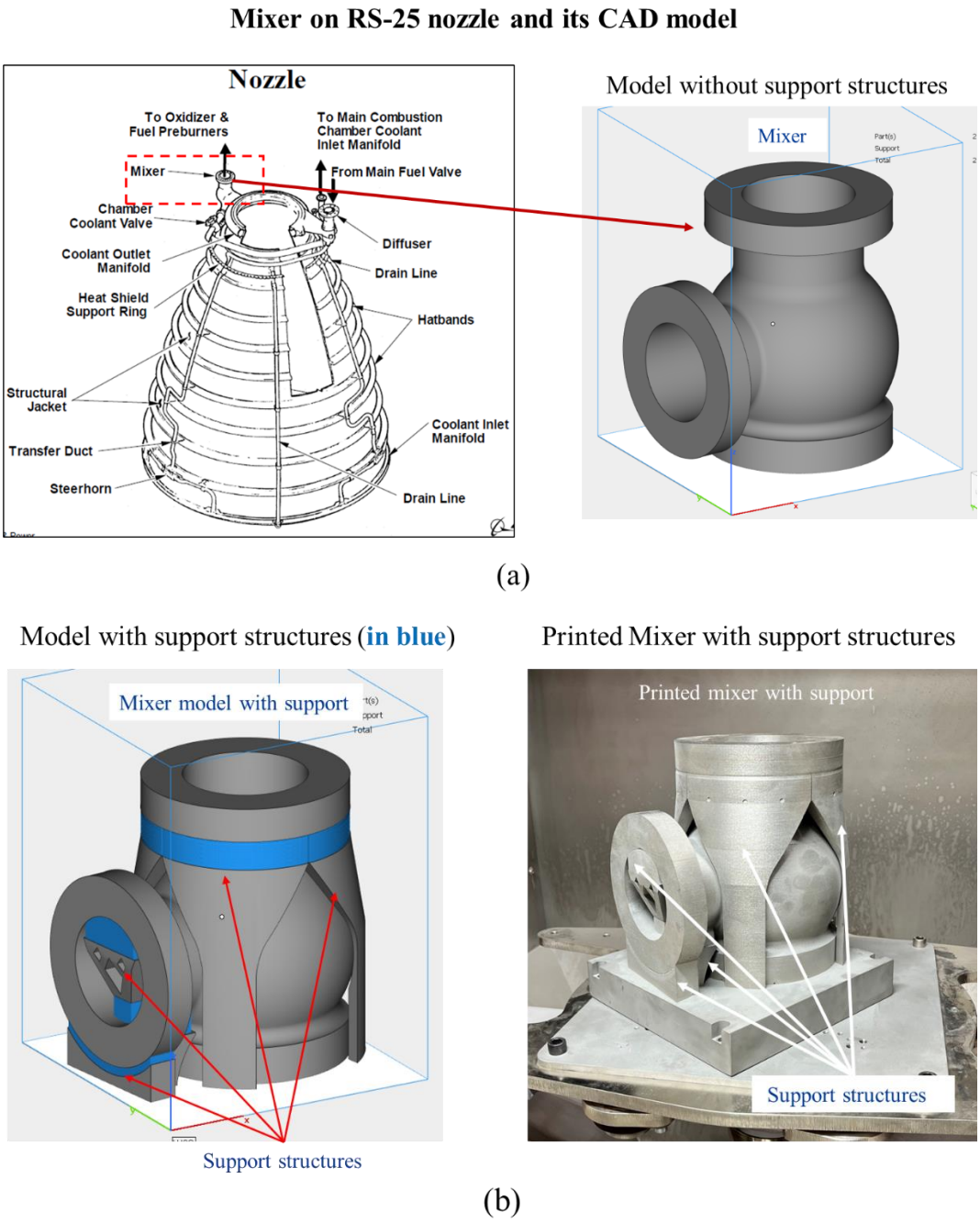

Figure 29. (a) Mixer component on the RS-25 nozzle and corresponding CAD model. (b) CAD model illustrating support structure design and the successfully printed component.

3.7.1 Fabrication of Lift-Off Seal Housing

Demonstration hardware fabrication focused on the RS-25 lift-off seal housing, which was successfully fabricated by L-PBF NASA HR-2 despite containing small unsupported internal flow passages that are traditionally difficult to manufacture. In the RS-25 LPFTP, the lift-off seal

provides static sealing during engine shutdown and controlled leakage during operation to maintain pressure balance and enable dynamic sealing. The lift-off seal housing contains two internal flow passages with a nominal diameter of 2.8 mm. These passages are difficult to fabricate using conventional machining and also present a significant challenge for L-PBF because of the unsupported downskin surfaces generated during fabrication [47, 48].

3.7.1.1 Parameter Design and Energy Density Levels

To evaluate the influence of laser energy input on internal channel quality, a series of builds was conducted using three parameter sets with systematically varied VED. The core and downskin laser parameters for each VED condition are summarized in Table 14. VED was adjusted through variations in scan speed and hatch spacing to assess the effect of energy input on melt pool behavior and downskin surface quality.

Table 14. L-PBF process parameter sets and scan strategy variables for lift-off seal wedges, including energy input–related parameters and hatch rotation strategy.

	Core Scan Parameter						**Downskin Scan Parameter**				
Specimens and ID	Parameter set	Laser Power (watt)	Scan Speed (mm/s)	Hatch Spacing (mm)	Layer Thickness (mm)	Core VED	Laser Power (watt)	Scan Speed (mm/s)	Hatch Spacing (mm)	Layer Thickness (mm)	Downskin VED
Wedge 1, 2	A	285	960	0.11	0.04	67.47	95	1100	0.1	0.04	21.59
Wedge 3, 4	B	285	1060	0.11	0.04	61.11					
Wedge 5, 6	C	285	1020	0.12	0.04	58.21					

All builds employed a new round internal channel path design with a teardrop-shaped inlet as shown in Figure 30. The teardrop ceiling is inclined at 45° from horizontal, creating a self-supporting overhang intended to reduce melt pool collapse and dross formation [48, 49]. The cut plan used for metallographic evaluation is presented in Figure 31. Samples were sectioned perpendicular to the channel centerline at five axial locations along each wedge.

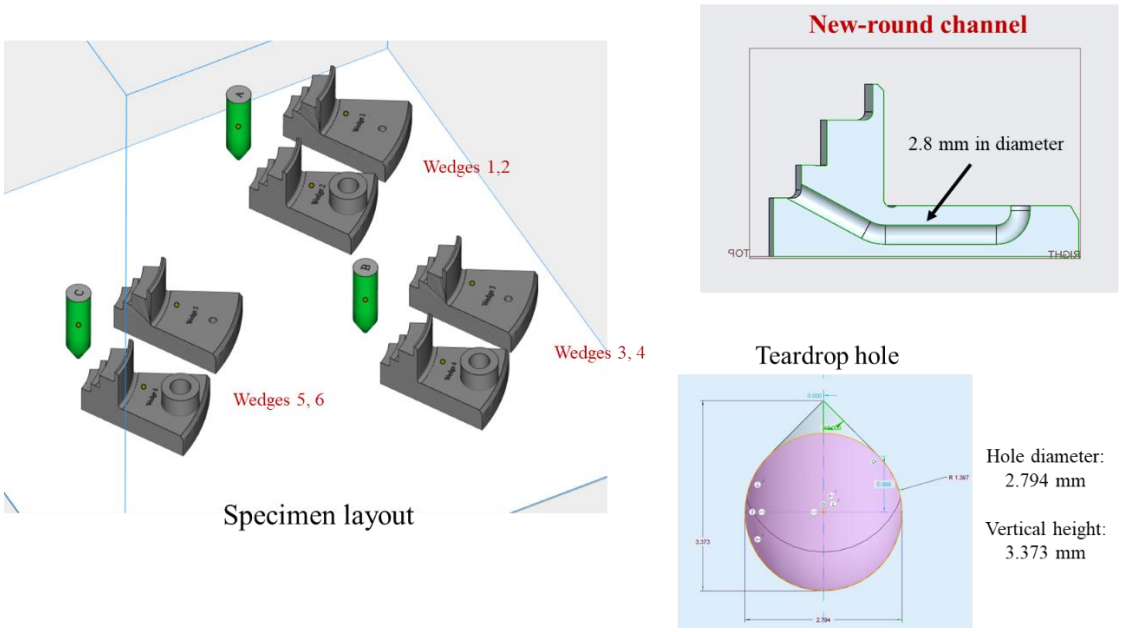

Figure 30. Layout and images of lift-off seal wedges, the new-round internal channel design, and teardrop-shaped inlet geometry.

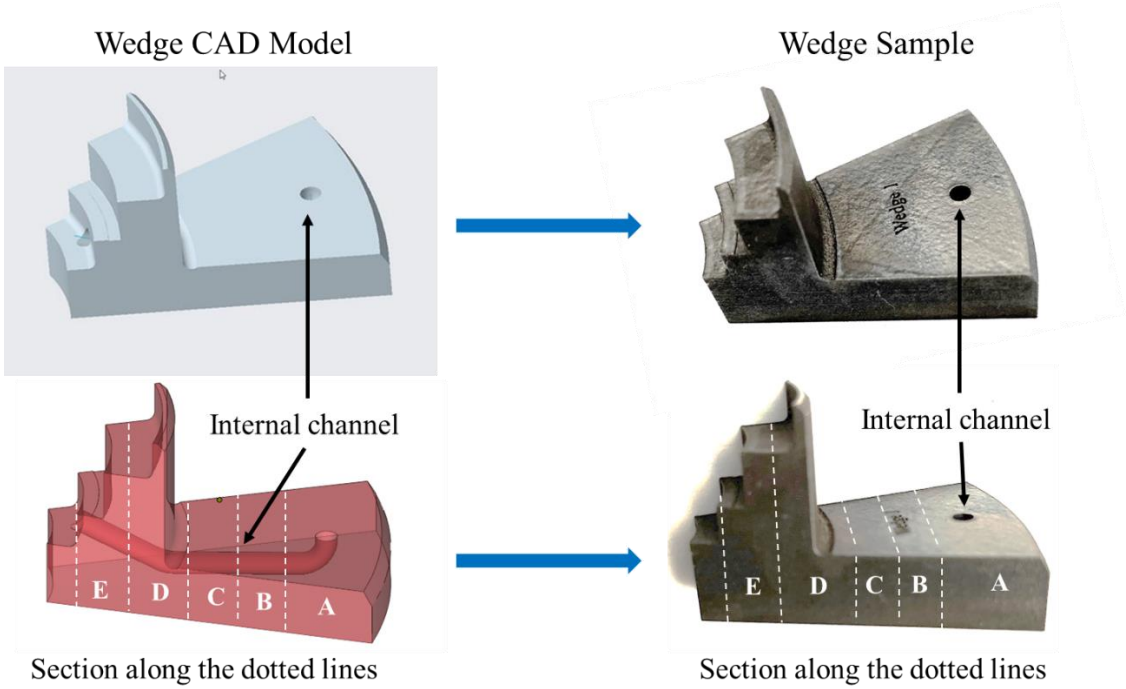

Figure 31. Cut plan for metallographic analysis. Samples were sectioned perpendicular to the channel centerline at five axial locations labeled as A, B, C, D, and E to evaluate internal channel quality and dimensional accuracy.

3.7.1.2 Effect of Volumetric Energy Density (VED) on Internal Channel Quality

Lift-off seal wedges were sectioned in two orientations to evaluate internal channel quality: longitudinally (parallel to the channel axis) and transversely (perpendicular to the channel centerline). The new-round channel incorporates a teardrop-shaped inlet geometry designed to improve support during fabrication.

Longitudinal sections (Figure 32) showed similar channel continuity and overall surface uniformity across all three parameter sets. Under all VED conditions, L-PBF NASA HR-2 exhibited excellent dimensional fidelity and very low porosity adjacent to the internal channels, indicating stable bulk consolidation. No gross channel collapse or blockage was observed along the channel length for any condition.

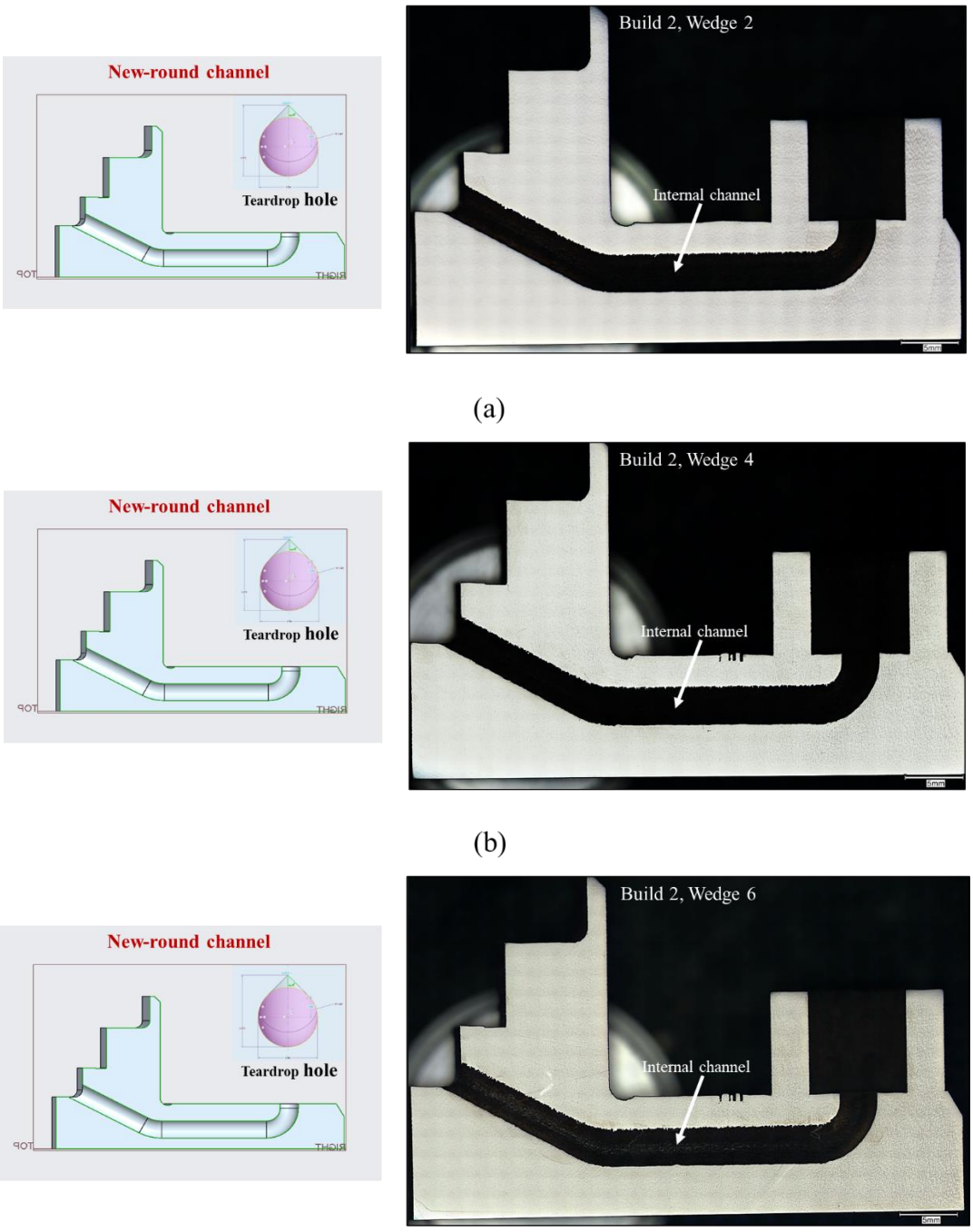

Figure 32. Longitudinal sections of lift-off seal wedges illustrating internal channel continuity and ceiling surface condition along the channel length for (a) Parameter Set A (high VED), (b) Parameter Set B (medium VED), and (c) Parameter Set C (low VED). The new round internal channel design has teardrop-shaped inlet geometry.

Cross-sectional views (Figure 33) revealed that across all conditions, excellent densification and minimal porosity were observed adjacent to the channels. Internal surface quality varied slightly with VED along the unsupported teardrop downskin surfaces. Because the nominal geometry and downskin parameters were identical across builds, observed differences are attributed to variations in the core process parameters.

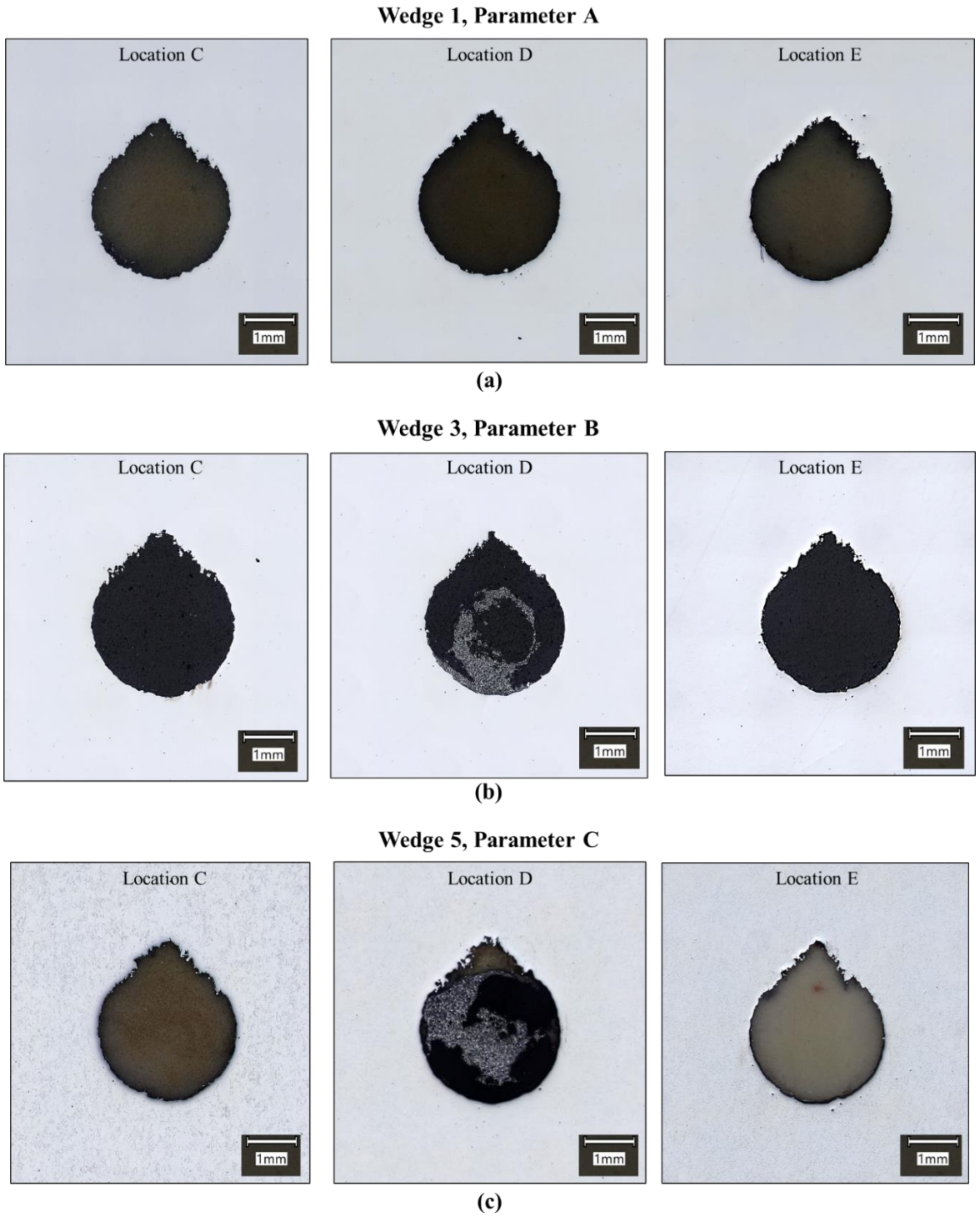

Figure 33. Cross-sectional views of lift-off seal wedges at locations C, D, and E showing the effect of VED on internal channel dimensional accuracy and surface quality: (a) Parameter Set A (high VED), (b) Parameter Set B (medium VED), and (c) Parameter Set C (low VED).

At the highest VED (Parameter A), higher energy input produced more unstable melt pools, leading to more pronounced downskin roughness. Downskin surface quality improved at the medium- and low-VED conditions (Parameter sets B and C). Overall, these results demonstrate that NASA HR-2 possesses a relatively broad and robust processing window for fabrication of small unsupported internal channels. Moderate reductions in VED enhance melt-pool stability and improve downskin surface quality while maintaining full densification. These findings establish practical processing guidelines for manufacturing lift-off seal channels by L-PBF.

3.7.1.3 Microstructural Features Associated with Downskin Surface Roughness (Sa)

Microstructural features associated with downskin Sa (Areal Surface Roughness) and melt pool instability were examined for Parameter Set A (Figure 34). The teardrop-shaped internal channel measured approximately 2.8 mm in the horizontal direction and 3.3 mm in the vertical direction, closely matching the nominal CAD dimensions of 2.794 mm × 3.373 mm. The channel at location E is oriented approximately 30° off horizontal.

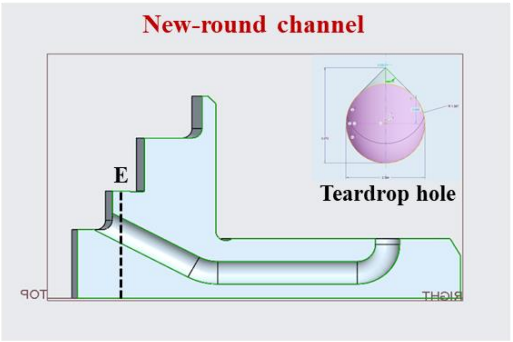

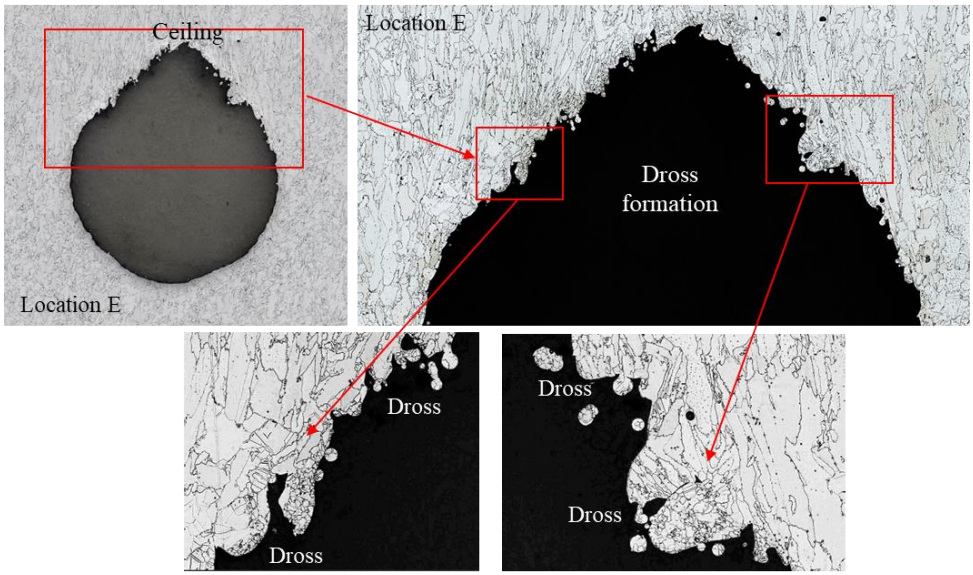

Figure 34. Close-up views of the internal teardrop-shaped channel ceiling fabricated using Parameter Set A, illustrating dross formation along the unsupported downskin surface. The channel at location E is oriented approximately 30° off horizontal. Bead-like protrusions and partially fused powder indicate melt pool sagging under downskin thermal conditions, while elongated columnar grains adjacent to the ceiling reflect heat-flow-controlled epitaxial solidification.

The observed dross morphology—characterized by bead-like protrusions and partially fused powder adhering to the ceiling—is consistent with melt pool instability and localized sagging under downskin conditions [47, 48]. The dross accumulation suggests intermittent sagging and collapse of molten material into the surrounding powder bed prior to solidification, producing the bead-like deposits along the channel ceiling.

The microstructure adjacent to the inclined ceiling shows elongated, upward-aligned columnar grains formed through epitaxial solidification during L-PBF. The inclined geometry promotes

directional heat extraction into the underlying solid material, generating steep thermal gradients that sustain columnar grain growth. These grains extend across multiple layers, indicating continuous epitaxial growth supported by stable thermal conduction paths. Although reducing VED slightly improved overall internal channel fidelity, the upper channel surfaces remained relatively rough under all processing conditions because of the inherently unsupported downskin geometry.

3.7.1.4 Effect of Internal Channel Path Design for Circular Channels

Based on the combined considerations of channel quality, dimensional accuracy, and process robustness, Parameter Set B was selected for all subsequent lift-off seal fabrication studies to fabricate additional lift-off seal wedges incorporating circular inlet holes and two internal channel path designs—a new-round path (constant-radius design with discrete horizontal segments) and a sweep-round path (continuously varying-radius design)—as shown in Figure 35. These designs were selected to isolate the influence of local overhang angle and thermal symmetry on internal channel surface quality under identical material and processing conditions.

	Core Parameter					Downskin Parameter				
Parameter Set	Laser Power (watt)	Scan Speed (mm/s)	Hatch Spacing (mm)	Layer Thickness (mm)	VED	Laser Power (watt)	Scan Speed (mm/s)	Hatch Spacing (mm)	Layer Thickness (mm)	VED
B	285	1060	0.11	0.04	61.11	95	1100	0.1	0.04	21.59

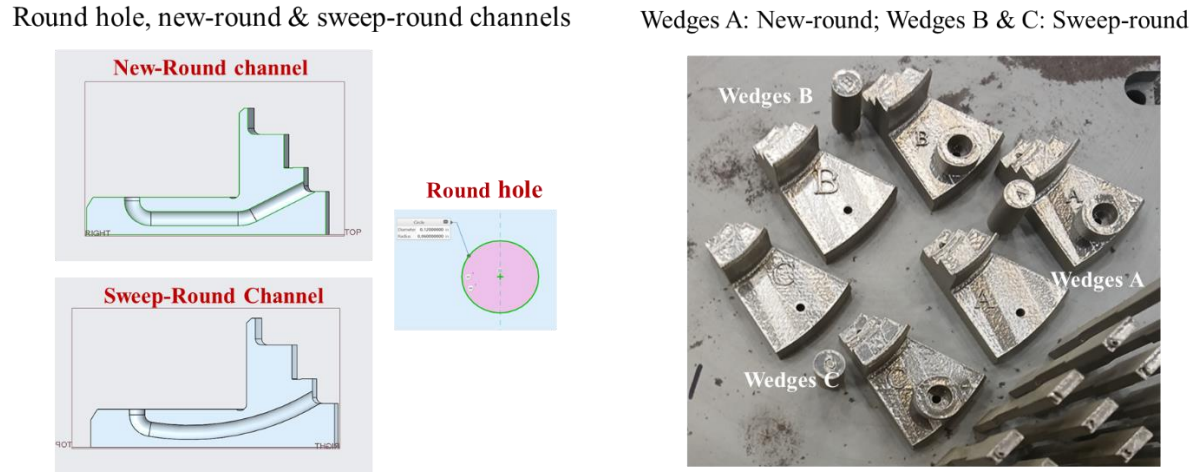

Figure 35. Fabrication of lift-off seal wedges with a circular inlet hole and two internal channel path designs: (a) new-round channel and (b) sweep-round channel. Core and downskin parameter regions are indicated.

3.7.1.5 New-Round Channel vs. Sweep-Round Channel Designs

Longitudinal sections were examined to evaluate internal channel surface quality along the full channel length (Figure 33) for both internal channel path designs. The new-round internal channel exhibited uniform surface morphology along the channel length, with good ceiling continuity and minimal localized thinning or material loss (Figure 36a).

In contrast, the sweep-round internal channel showed localized thinning and material loss distributed along extended portions of the channel length (Figure 36b). Although the sweep-round design avoids a strictly horizontal ceiling, it maintains shallow, continuously varying ceiling angles over long axial distances. These geometric conditions appear to promote less stable melt-pool behavior during downskin formation, resulting in localized sagging and surface irregularities. Over successive layers, these effects accumulate and lead to progressive ceiling degradation, dimensional variation, and nonuniform internal surface morphology [48, 49]. Overall, the new-round channel consistently outperformed the sweep-round design, producing more uniform ceiling morphology, improved dimensional stability, and more repeatable internal surface quality despite containing extended horizontal channel segments.

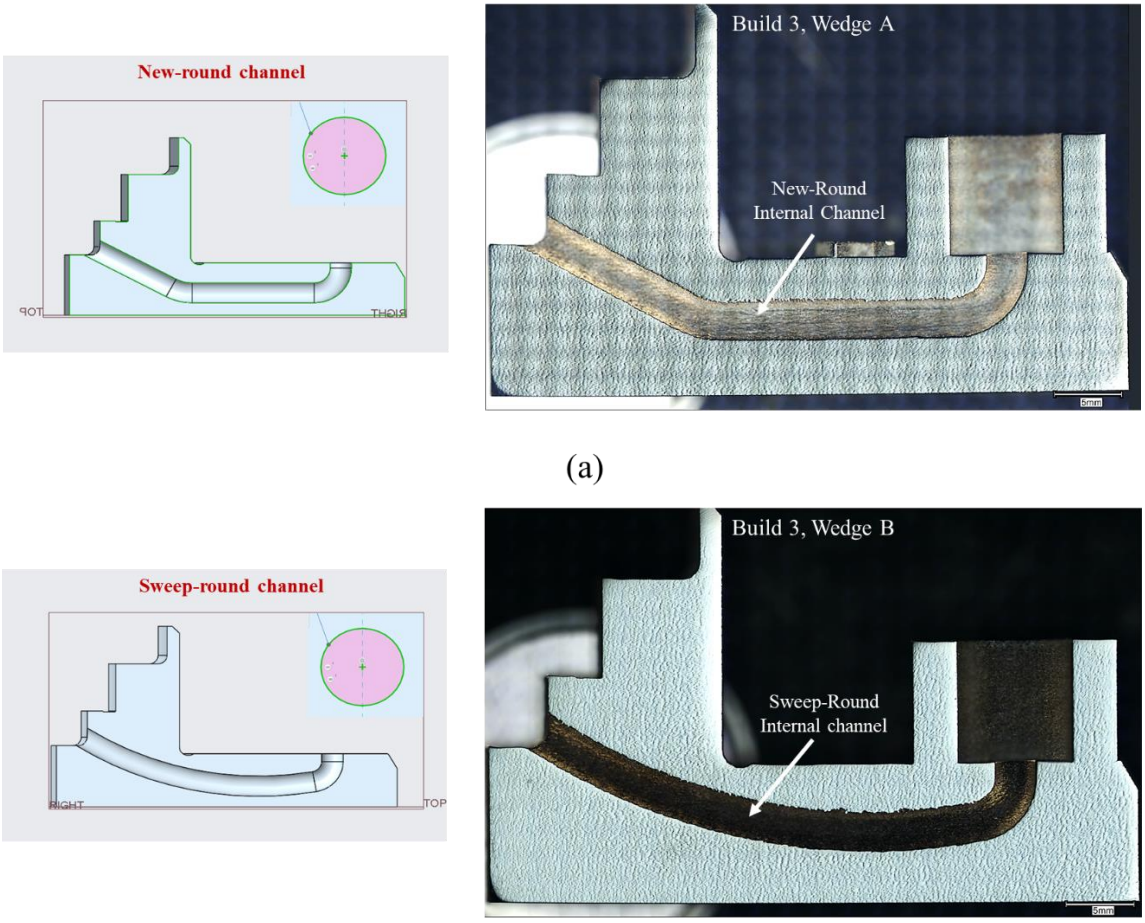

Figure 36. Longitudinal sections of lift-off seal wedges highlighting circular internal channel path designs: (a) new-round channel and (b) sweep-round channel. Each channel was sectioned along its longitudinal axis. Overall, the longitudinal results show that the new-round design provides superior longitudinal ceiling quality compared to the sweep-round design, despite containing extended horizontal segments.

Cross-sectional analysis further supports the longitudinal observations regarding the influence of internal channel path design on downskin stability. Three cross-sectional samples were extracted from each wedge to evaluate internal channel dimensional accuracy and surface integrity (Figure 37).

For both path designs, cross-sectional views revealed flattened or slightly sagged channel ceilings, consistent with melt pool deformation under unsupported downskin formation. However, the extent and uniformity of the distortion differed between the two designs. The new-

round channels exhibited more uniform ceiling profiles with limited variation among cross-sectionallocations, indicating more consistent and repeatable fabrication of the channel ceiling. In contrast, the sweep-round channels showed greater variability in ceiling shape and localized thinning along the channel length, indicating less consistent downskin formation and greater geometric variability. Collectively, the longitudinal and cross-sectional observations demonstrate that the new-round channel path provides a more robust design for fabricating small unsupported internal channels in L-PBF NASA HR-2.

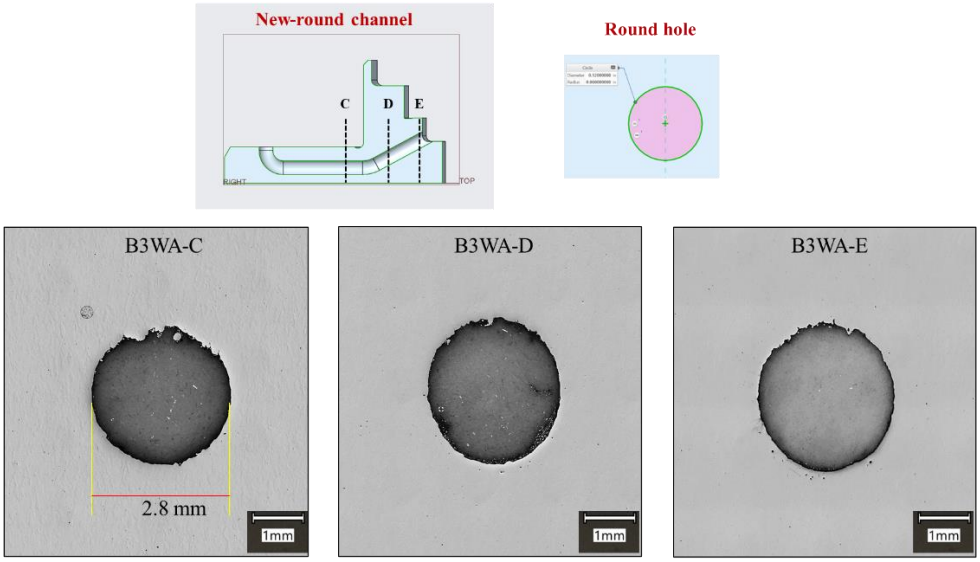

(a)

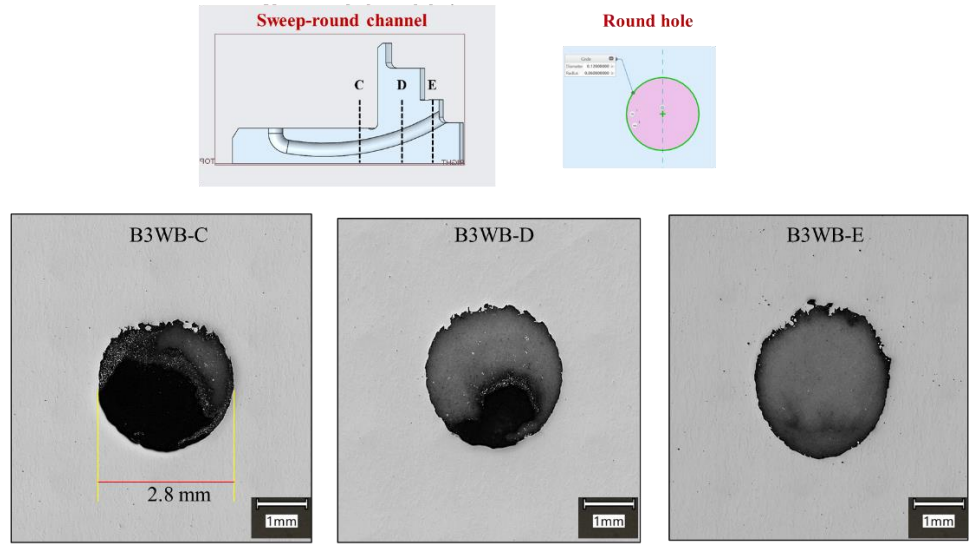

(b)

Figure 37. Cross-sectional views of lift-off seal wedges with circular internal channels illustrating the effect of channel path design on dimensional accuracy and surface quality: (a) new-round channel and (b) sweep-round channel. Sections were taken perpendicular to the channel centerline at three axial locations. Overall, the new-round design provides improved dimensional stability and internal surface consistency compared to the sweep-round design.

3.7.1.6 Manufacturability Implications

Lift-off seal wedges with 2.8-mm-diameter internal channels were fabricated to evaluate both path designs using relatively small internal channels that are sensitive to the geometric and

process limitations of L-PBF. For these 2.8-mm-diameter channels, melt-pool stability and geometric repeatability can significantly affect surface quality and dimensional accuracy. The new-round design provides a clear manufacturability advantage, exhibiting improved ceiling integrity, reduced Sa, and more consistent cross-sectional geometry compared to the sweep-round design. Although the sweep-round design is intended to improve fluid flow by providing a smoother nominal channel path, at a 2.8 mm diameter the as-built surface condition and dimensional fidelity are expected to dominate pressure-drop behavior. As a result, the increased Sa and geometric variability of the sweep-round channels are expected to outweigh any theoretical hydraulic benefit.

3.7.1.7 Effects of Hole Shape - Teardrop vs. Round

Round and teardrop internal hole geometries were evaluated for small (2.8 mm diameter) internal channels fabricated by L-PBF. Teardrop holes are commonly used in additive manufacturing to reduce unsupported horizontal overhangs and mitigate ceiling collapse [48-50].

In this study, round holes produced using the new-round channel path and optimized downskin parameters exhibited minimal ceiling collapse, good circularity, and relatively smooth internal surfaces. These results indicate that melt pool stability and heat dissipation at the channel ceiling were sufficient under the selected process conditions, eliminating the need to compensate for unsupported overhangs through the use of a teardrop geometry.

From a manufacturing standpoint, the teardrop geometry did not provide a measurable improvement in build quality for this configuration. While it modifies local overhang conditions, it introduces geometric asymmetry without reducing ceiling roughness or distortion. As a result, it increases design complexity without offering a clear manufacturability benefit under the current L-PBF conditions.

From a fluid-flow perspective, a teardrop hole with a cross-sectional area similar to that of a round hole has a larger wall surface in contact with the fluid, which increases flow resistance and pressure drop [51]. Overall, the conventional circular hole provided the best combination of manufacturability, dimensional accuracy, and hydraulic performance. Under the optimized HR-2

processing conditions developed in this study, modifying the channel to a teardrop geometry was unnecessary. Teardrop holes should therefore be considered for larger channels or more severe unsupported overhang conditions where ceiling collapse, downskin deformation, or surface roughness becomes limiting..

3.7.2 Summary of Lift-Off Seal Fabrication

The lift-off seal fabrication study demonstrated the excellent manufacturability of L-PBF NASA HR-2 for small unsupported internal channels, successfully producing nominal 2.8 mm-diameter passages with excellent densification and dimensional fidelity. Moderate reductions in volumetric energy density improved melt-pool stability and downskin surface quality, establishing a practical processing window for unsupported internal features.

Among the channel designs evaluated, the new-round path consistently produced superior ceiling integrity, dimensional stability, and surface quality compared with the sweep-round design. Furthermore, conventional circular holes fabricated using the optimized processing parameters exhibited excellent build quality, demonstrating that teardrop hole geometries were unnecessary for this application. Collectively, these results establish practical processing and design guidelines for manufacturing complex HR-2 turbomachinery hardware containing small internal flow passages by L-PBF.

4.0 Conclusions

1. NASA HR-2 exhibited robust L-PBF printability with consistently low porosity across a broad processing window, with a hatch spacing of 0.11 mm providing the most stable consolidation behavior. HIP further reduced residual porosity in well-consolidated builds, whereas irregular lack-of-fusion defects exhibited only limited closure. Based on porosity, microstructure, surface quality, and process stability, parameter sets 285-11-P5 and 285-11-P6 were selected for fabrication of mechanical test specimens and demonstration hardware.

2. The tensile behavior of L-PBF NASA HR-2 was strongly influenced by aging treatment and test temperature. A primary aging temperature of 1325 °F was required to consistently achieve the minimum yield strength of 95 ksi. HR-2 exhibited excellent cryogenic tensile performance, with simultaneous increases in strength and ductility under LH_2 conditions. Although tensile properties remained favorable through intermediate temperatures, the marked reduction in ductility above 1200 °F suggests a practical upper temperature limit for structural applications.

3. Room-temperature tensile testing of L-PBF NASA HR-2 in 5-ksi gaseous hydrogen produced only minor reductions in yield and ultimate tensile strengths relative to air, while fracture elongation was fully retained or modestly increased. Hydrogen-assisted damage was limited to shallow surface cracking, with bulk fracture remaining predominantly ductile and free of intergranular failure. Overall, hydrogen-assisted damage remained highly localized and did not degrade bulk tensile performance, confirming strong resistance to hydrogen embrittlement.

4. The high-cycle fatigue response of machined L-PBF HR-2 was governed primarily by stress amplitude and mean stress. Fatigue failure was dominated by crystallographic slip-controlled crack initiation, with no evidence of defect-driven initiation. Relative to SLM IN718 and wrought A-286, HR-2 exhibited higher fatigue resistance than A-286 and improved consistency under fully reversed loading compared with SLM IN718.

5. L-PBF NASA HR-2 was successfully transitioned from material development to fabrication of representative RS-25 turbomachinery hardware, including a lift-off seal housing, a single-piece rotor, and a mixer component. The lift-off seal study demonstrated reliable fabrication of small unsupported internal channels (~2.8 mm diameter) with excellent densification and dimensional fidelity. A robust processing window was established through optimized volumetric energy density and downskin parameters, while the new-round channel path consistently outperformed the sweep-round design. Conventional circular holes also exhibited excellent build quality, demonstrating that teardrop hole geometries were unnecessary under the optimized processing conditions. These findings establish practical processing and design guidelines for manufacturing complex HR-2 turbomachinery components by L-PBF.

6. Future work will focus on advancing L-PBF NASA HR-2 toward implementation in flight-relevant aerospace hardware. Additional demonstration components, including an interpropellant seal (IPS) housing for the RS-25 high-pressure oxidizer turbopump (HPOTP), will be fabricated to further evaluate manufacturing capability and design limits. Additional mechanical property data—including fracture toughness (KIC), fatigue crack growth rate (da/dN), and LCF—will be generated to support qualification for hydrogen-sensitive liquid rocket engine applications.

Overall, this work demonstrates that NASA HR-2 is a highly manufacturable hydrogen-resistant superalloy for laser powder bed fusion. Its robust printability, excellent mechanical performance in air and hydrogen, and successful fabrication of representative RS-25 hardware provide a strong foundation for future qualification and implementation in liquid rocket engine applications.

References

1. Chen, P.S., Panda, B., and Bhat, B.N., "NASA HR-1, A New Hydrogen Resistant Fe-Ni Base Superalloy," Proceedings of the Fifth International Conference on the Effect of Hydrogen on the Behavior of Materials, edited by A.W. Thompson and N.R. Moody, Moran, WY, Sept. 11–14, 1994, The Minerals, Metals & Materials Society, 1996, pp. 1011–1020.

2. Chandler, W. T. “Hydrogen-Environment Embrittlement and Its Control in High Pressure Hydrogen/Oxygen Rocket System,” Advanced Earth-to-Orbit Propulsion Technology of NASA Conference Publication 2437, no. 2, (1986).

3. Katsarelis, C.C., Chen, P.S., Gradl, P.R., Protz, C.S., Jones, Z., Ellis, D.L., and Evans, L., "Additive Manufacturing of NASA HR-1 for Liquid Engine Component Applications," JANNAF Conference, Dec. 2019.

4. Chen, P.S., Katsarelis, C.C., Medders, W.M., and Gradl, P.R., "Segregation Evolution and Diffusion of Titanium in DED NASA HR-1," NASA/TM-20210013649, May 2021.

5. Gradl, P.R., Thomas, W.T., Christopher, S.P., Colton, C.C., and Chen, P.S., "Process Development and Hot-Fire Testing of Additively Manufactured NASA HR-1 for Liquid Rocket Engine Applications," AIAA Propulsion and Energy Forum, 2021.

6. Chen, P.S., Katsarelis, C.C., Medders, W.M., Gradl, P.R., and Su, C.H., "Development of Directed Energy Deposited NASA HR-1 to Optimize Properties for Liquid Rocket Engine Applications," NASA/TM-20230006075, Apr. 2023.

7. Chen, P.S., Fullen, M.D., Watwood, W.C., Rupp, B.L., Medders, W.M., Colton, C.C., Gradl, P.R., "Effects of Strain Rate and Surface Finish on Tensile Properties in High Pressure Hydrogen—A Case Study for LP-DED NASA HR-1," NASA/TM-20230008831, June 2023.

8. Gradl, P.R., Mireles, O.R., Katsarelis, C.C., Smith, T.M., Sowards, J.W., Park, A.M., Chen, P.S., Tinker, D.C., Protz, C.S., Teasley, T.W., Ellis, D.L., Kantzos, C.A., "Advancement of Extreme Environment Additively Manufactured Alloys for Next-Generation Space Propulsion Applications," *Acta Astronautica*, Vol. 211, 2023, pp. 483–497.

9. Gradl, P.R., Tinker, D.C., Park, A.M., Mireles, O.R., Garcia, M.B., Wilkerson, R.P., and McKinney, C.G., "Robust Metal Additive Manufacturing Process Selection and Development for Aerospace Components," *Journal of Materials Engineering and Performance*, Vol. 31, 2022, pp. 7735–7753. DOI: 10.1007/s11665-022-06850-0.

10. Chen, P.S., Rupp, B.L., Katsarelis, C.C., Andreev, D.Y., Su, C.H., and Culver, A.G., "Development of Laser Powder Bed Fusion NASA HR-2 for Hydrogen Sensitive Liquid Rocket Engine Applications," AIAA SciTech Forum, 6-10 January 2025, Orlando, FL.

11. Chen, P.S., Rupp, B.L., Katsarelis, C.C., Andreev, D.Y., Su, C.H., and Culver, A.G., "Development of the NASA HR-2 Superalloy for Hydrogen-Sensitive Liquid Rocket Engines via Laser Powder Bed Fusion," NASA/TP-20250006708, July 2025.

12. Ozbilen, S. "Satellite formation mechanism in gas atomised powders," *Powder Metallurgy* 42(1), pp. 70–78, January 1999.

13. Keshavarzkermani, A., Esmaeilizadeh, R., Ali, U., Enrique, P., Mahmoodkhani, Y., Zhou, N.Y., Bonakdar, A., and Toyserkani, E., "Controlling Mechanical Properties of Additively Manufactured Hastelloy X by Altering Solidification Pattern During Laser Powder-Bed Fusion," Materials Science and Engineering A, Vol. 762, 2019, p. 138081.

14. Hibino, S., Fujimitsu, K., Azuma, M., Ishimoto, T., Nakano, T. "Effects of Recrystallization on Tensile Anisotropic Properties for IN738LC Fabricated by Laser Powder Bed Fusion," Crystals, Vol. 12, 2022, p. 842. DOI: 10.3390/cryst12060842.

15. Herzog, D., Seyda, V., Wycisk, E., and Emmelmann, C., "Additive Manufacturing of Metals," Acta Materialia, Vol. 117, 2016, pp. 371–392. https://doi.org/10.1016/j.actamat.2016.07.019

16. Habeeb, N.V.V., Islam, R., and Chou, K., "Influence of Pre- and Post-Contouring Strategies to Downskin Sloped Surfaces in Laser Powder-Bed Fusion (L-PBF) Additive Manufacturing," Materials, Vol. 17, 2024, Article 2639. DOI: 10.3390/ma17112639.

17. *Aydogan, B., Chou, K., "A Numerical Study of Topography and Roughness of Sloped Surfaces Using Process Simulation Data for Laser Powder Bed Fusion,"* Materials, Vol. 17, No. 23, 2024, Article 5955. DOI: 10.3390/ma17235955.

18. Shange, M., Yadroitsava, I., du Plessis, A., and Yadroitsev, I., "Roughness and Near-Surface Porosity of Unsupported Overhangs Produced by High-Speed Laser Powder Bed Fusion," 3D Printing and Additive Manufacturing, Vol. 9, No. 4, 2022, pp. 288–300. DOI: 10.1089/3dp.2020.0097.

19. Yang, Z., Kim, J., Lane, B., Lu, Y., "Measuring Overhang Down-Skin Dross Depth and the Inter-Dependency on Melt Pool for Laser Powder Bed Fusion Additive Manufacturing," ASME 2024 19th International Manufacturing Science and Engineering Conference, June 17–21, 2024, Knoxville, Tennessee, USA. Paper No. MSEC2024-124322, V001T01A020. https://doi.org/10.1115/MSEC2024-124322

20. Sames, W.J., List, F.A., Pannala, S., Dehoff, R.R., and Babu, S.S., "The Metallurgy and Processing Science of Metal Additive Manufacturing," *International Materials Reviews*, Vol. 61, No. 5, 2016, pp. 315–360. DOI: 10.1080/09506608.2015.1116649.

21. Adomako, N.K., Haghdadi, N., and Primig, S., "Electron and Laser-Based Additive Manufacturing of Ni-Based Superalloys: A Review of Heterogeneities in Microstructure and Mechanical Properties," *Materials & Design*, Vol. 223, 2022, Article 111245.

22. Fencheng, L., L. Xin, Y. Gaolin, et al., “Recrystallization and its influence on microstructures and mechanical properties of laser solid formed nickel base superalloy Inconel 718,” *Rare Metals*, Vol. 30, no. 1, pp. 433–438, doi:10.1007/s12598-011-0319-0, March 2011.

23. Zhang, F, L.E. Levine, A.J. Allen, et al., “Effect of heat treatment on the microstructural evolution of a nickel-based superalloy additive-manufactured by laser powder bed fusion,” *Acta Materialia*, Vol. 152, pp. 200–214, June 2018.

24. Cao, J., F. Liu, X. Lin, et al., “Effect of overlap rate on recrystallization behaviors of Laser Solid Formed Inconel 718 superalloy,” *Optics & Laser Technology*, Vol. 45, pp. 228–235, February 2013.

25. Weaver, J.S., and Rosenthal, I., "Understanding Anisotropic Tensile Properties of Laser Powder Bed Fusion Additive Metals: A Detailed Review of Select Examples," NIST Advanced Manufacturing Series 100-44, National Institute of Standards and Technology, 2024.

26. Wang, G.L., Liu, J.L., Liu, J.D., Wang, X.G., Zhou, Y.Z., Sun, X.D., Zhang, H.F., Jin, T., “ Temperature dependence of tensile behavior and deformation microstructure of a Re-containing Ni-base single crystal superalloy.“ Materials & Design, Vol. 130, 2017, pp. 131–139.

27. *Reed, R.C., The Superalloys: Fundamentals and Applications, Cambridge University Press, Cambridge, UK, 2006.*

28. Ahmad, N., Ghiaasiaan, R., Gradl, P.R., Shao, S., and Shamsaei, N., "Revealing Deformation Mechanisms in Additively Manufactured Alloy 718: Cryogenic to Elevated Temperatures," Materials Science and Engineering A, Vol. 849, Article 143528, 2022.

29. Poudel, A., P.R. Gradl, S. Shao, N. Shamsaei, “Tensile deformation behavior of laser powder direct energy deposited Inconel 625: Cryogenic to elevated temperatures,“ *Materials Science & Engineering* A 889, 145826, 2024.

30. Nordström, J., R. Siriki, M. Calmunger, J. Moverare, G. Chai, “TWIP and Fracture Behavior in the Superalloy 625 at Room and Cryogenic Temperatures,” *Procedia Structural Integrity* 23, pp. 457–462, 2019.

31. Anjaria, D., M. Heczko, R.L. Black, C. Bean, M.A. Reynolds, K. Zhang, D. Texier, V. Valle, M.J. Mills, D.C. Pagan, J.C. Stinville, “Plastic deformation delocalization at cryogenic temperatures in a nickel-based superalloy,” *Acta Materialia* 276, 120106, 2024.

32. Wang, Y., J. He, P. Hu, C. Xiao, X. Wang, “Exceptional cryogenic tensile properties of K4169 superalloy by micro-grain casting process,” *Materials & Design* 236, 112450, 2023.

33. Chalapathi, D., J. Nordström, R. Siriki, L. Lautrup, G. Chai, A. Kanjarla, “Deformation twinning and the role of stacking fault energy during cryogenic testing of Ni-based superalloy 625,” *Materials Science & Engineering* A 898, 146404, 2024.

34. Nordström, J., Z. Dong, L. Lautrup, R. Siriki, L. Vitos, J. Moverare, M. Calmunger, G. Chai, “Temperature study of deformation twinning behavior in nickel-base Superalloy 625,” *Materials Science & Engineering* A 907, 146628, 2024.

35. Tirunilai, A.S., Hanemann,T., Weiss, K.-P., Freudenberger, J., Heilmaier, M., Kauffmann, A., “Dislocation-based serrated plastic flow of high entropy alloys at cryogenic temperatures,” Acta Materialia 200 (2020) 980–991.

36. Damm, N., Lukas, M., Platl, J., Drexler, A., Eichinger, M., Eskinja, M., Mori, G., Simon, Z., Scheerer, M., Marsoner, S., Razumovskiy, V.I., “Hydrogen–Dislocation Interactions at Cryogenic Temperatures: Serrated Yielding and Embrittlement Resistance in High-Strength Austenitic Alloys,” Materials 2025, 18, 5109.

37. Klopp, W. D., “A286,” *Aerospace Structural Metals Handbook*, March 1987.

38. Bedford, A., and Liechti, K. M., *Mechanics of Materials*, Prentice Hall, 2000. ISBN: 9780201895520.

39. *Dowling, N.E., Mechanical Behavior of Materials: Engineering Methods for Deformation, Fracture, and Fatigue, 2nd ed., Prentice Hall, Upper Saddle River, NJ, 1999.*

40. Kim, D., Jiang, R., Sinclair, I., Reed, P. “Microstructural influences on fatigue crack initiation and early propagation in Ni-based superalloys,” Materials Science and Technology, 38(14), 1081–1094, 2022.

41. Smith, K.N., Watson, P., Topper, T.H. “A stress-strain function for the fatigue of metals,” Journal of Materials, 5, 767–778, 1970.

42. Dodaran, M.S., Muhammad, M., Shamsaei, N., Shao, S. “Synergistic effect of microstructure and defects on the initiation of fatigue cracks in additively manufactured Inconel 718,” International Journal of Fatigue, 162, 107002, 2022.

43. NASA Marshall Space Flight Center (MSFC), High-Cycle Fatigue Datasets for SLM 718 and Wrought A286, Internal Materials Database, Unpublished Engineering Data, Huntsville, AL, USA, accessed May 2026.

44. Polák, J., Maná, J. “Initiation of stage I fatigue cracks – experiments and models,” Procedia Engineering, 101, 386–394, 2015.

45. Suresh, S., Fatigue of Materials, 2nd ed., Cambridge University Press, Cambridge, 1998.

46. Stephens, R. I., Fatemi, A., Stephens, R. R., & Fuchs, H. O., Metal Fatigue in Engineering, 2nd Edition, Wiley, 2000.

47. Herzog, D., Asami, K., Scholl, C., Ohle, C., Emmelmann, C., Sharma, A., Markovic, N., and Harris, A. “Design guidelines for laser powder bed fusion in Inconel 718,“ J. Laser Appl. 34, 012015 (2022); https://doi.org/10.2351/7.0000508

48. Feng, S., Chen, S., Kamat, A.M., Zhang, R., Huang, M., Hu, L. “Investigation on shape deviation of horizontal interior circular channels fabricated by laser powder bed fusion,” Additive Manufacturing 36 (2020),101585; https://doi.org/10.1016/j.addma.2020.101585

49. Wilson, N., Gupta, M., Mazur, M., Patel, M.J., Nguyen, V., Gulizia, S., Cole, I.S. “Analysis of self-supporting conformal cooling channels additively manufactured by hybrid directed energy deposition for IM tooling,” The International Journal of Advanced Manufacturing Technology (2024) 132:421–441; https://doi.org/10.1007/s00170-024-13291-7

50. Gibson, I., Rosen, D.W., Stucker, B., and Khorasani, M., *Additive Manufacturing Technologies*, 4th ed., Springer, 2021.

51. Islam, S.A., Hao, L., Javaid, Z., Xiong, W., Li, Y., Jamil, Y., Chen, Q., Han, G., "Surface Roughness of Interior Fine Flow Channels in Selective Laser Melted Ti-6Al-4V Alloy Components,” Micromachines **2024**, 15(3), 348; https://doi.org/10.3390/mi15030348